Contents

Chapter 1

Introduction

In quantum cryptation experiments single photon detectors are needed. The requirements to these detectors does not make them commercially available even though its parts are. The objective of this master thesis is to design, build and test a single photon detector(SPD). The detector is an avalanche photo diode(APD) carefully selected by Mr. Hjelme. Since *single photons* are to be detected the APD must have a low dark current and need to be cooled in liquid nitrogen at about 77K. Because of this a cryostat must be made. The basics of how circuitry should be made is published in different papers. However, these circuit are mostly designed for low frequency only and need improvement. It's also decided to build everything(except the cooling section) into a Vero rack.

The basics of quantum cryptation and some aspects of cryptography is presented in chapter 2. Chapter 3 describes the physics of the APD and this is used in chapter 5 where some models for evaluating the APD is made. Chapter 4 describes the laser which is used to provide single photons. In chapter 6 a set of measurements made this summer are analyzed. The settings and circuits for the experiment in chapter 8 are described in chapter 7. The experiment is based on the theory in previous chapters and the preliminary measurements. Data sheets of components and data from the experiments are found in the Appendix.

Chapter 2

Quantum cryptation

There has been and is developed a number of different ways to protect sensitive information. The fundamentals of doing this are based on various theories, but the bottom line is that even though someone got hold of the encrypted message the information should still be useless. This chapter will give a brief introduction to some aspects cryptation and present a radical new approach called quantum cryptation(QC).

2.1 Cryptation

2.1.1 History

The art of cryptography began at least 2500 years ago. The research and development of cryptography were motivated by the diplomacy and on-going wars. Both "institutions" were in need of handing over messages in privacy. Most of the early chipers were, at todays standards, very simple to dechiper. A message to Julius Caesar could have been: "Aqtstr gzr z jmhed" which turns into "Brutus has a knife" simply by shifting all letters in the chipertext once to the right in the alphabet. However, it is safe to say that cryptography as used today is developed in the last decades.

An unbreakable chiper was invented in 1918, and not until the 1940's proved breakable. Another cipher used by the Germans, later on the cryptogram called the Zimmermann Note, was broken in 1917. Around this time the Vernam chiper was invented which was the first truly unbreakable code.

It was in the mid-70 that cryptography became of rising academic interest when Stanford Researchers discovered the principle of public-key cryptation. Soon after, in 1977 MIT scientists Rivest, Shamir and Adleman devised a practical implementation, which they called RSA. Chipers based on the RSA-

theory are today widely employed.

2.1.2 Cryptographic services and primitives

When sending a message the sender and receiver must consider a number of factors to make a safe transaction. These considerations are of course given by the nature of the message. Three major factors are data integrity, data origin authentication and data confidentiality.

Data integrity and data origin authentication are somewhat related. One would be meaningless without the other. It does not help to know that the message is not tampered with unless noone can assure it's sent by the right person and vise versa. Usually line tapping is only a matter of cost and most communication systems does not support any kind of protection as here mentioned. An experienced computer easily tap into transmitted messages over e.g. internet. With data confidentiality we try to protect the contents of a message from a third part. Now a days this is important also in banking and medical care.

Several cryptographic primitives are used to realize the above services. Basically there are two kinds of encryption schemes; symmetrical and asymmetrical. The symmetrical is by far the oldest. The same key is used both to enchiper and dechiper a message. The best known chiper in this category is the Data Encryption Standard(DES) which uses a 56-bit key. Improved versions of DES are made. Asymmetric or public key chipers are the most resent tools. Two different keys are used. One (public) key can enchiper a message but not vise versa. To dechiper a private key is needed. Thereby the name asymmetric. The already mentioned RSA system is one of most popular.

2.1.3 Security

For most purposes the level of confidence for commonly used chipers are sufficient. However, it's estimated that the DES 56-bit chiper can be broken in one day by searching for all possible values of the key. This operation takes an investment of about 200000 USD and some pairs of plaintext and chipertext. Also the RSA is vulnerable to exhaustive attacks. A system requiring safety for more than a few month requires a key of 768 and 1024 bits.

There exists other chipers that never have been proved broken. Bot nor proved safe either. In strict mathematical sense the systems widely used are not secure. It's only a matter of effort, resources and of course time. Inadequate computer power is therefore the factor most chipers relies on.

2.2 quantum cryptation

2.2.1 Introduction

Quantum cryptation (QC) offers a new approach to the matter of cryptography. Individual photons are employed taking advantage of Heisenberg's uncertainty principle stating that any measurement will unavoidable alter properties. This disturbance induced an eavesdropper will alert the legitimate users causing them to reject the exchanged message. This allows users of the QC channel to exchange messages with a provable security embedded in the fundamental laws of physics.

The idea of QC was born in the late 1960s when Stephen Weisner wrote an article called "Conjungate Coding". But is was not until 20 years later that the first successful experiment was conducted by Bennett and Brassard in 1984. Since then several institutions have reported QC over tens of kilometers.

2.2.2 System configuration

The first experiments were conducted based on a polarizing key. Lately it is realized that a phase key is more practical and more cost efficient. Phase key is also what NTNU and Telenor FoU will use. The experimental setup that will be used is based on the Mach-Zender interferometers shown in fig. 2.1 .

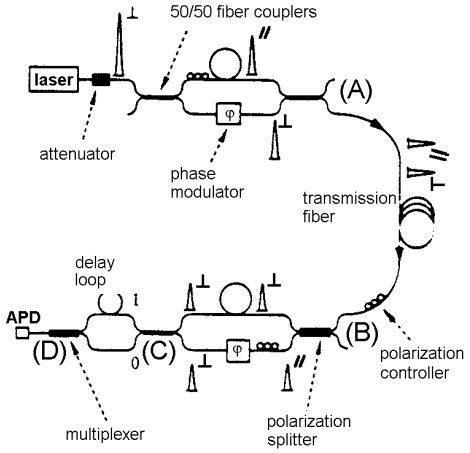

Figure 2.1: Marand-Townsend interferometric quantum cryptation scheme.

The heart of the systems are the two interferometers at the laser and the APD. In cryptography the sender(laser) and receiver(APD) is often referred

to as respectively Alice and Bob, and so do we. Alice and Bob can adjust their interferometers individually at four different phases and as strange as it sounds the setup can make single photons interfere. By adding some polarization devices the efficiency of the system can be improved so that the waves always chooses adjacent paths in the two interferometers.

2.2.3 Analysis of interferometers

Lets assume the light, for considerations of convenience, to be perfectly monochromatic. The real light is polychromatic, but the point is illustrated anyway. Single photon interference can be explained by the wave model of the light. The laser emitts a light pulse into an attenuator. Then in Alices interferometer the wave is split in two. One arm is equipped with a polarization controller. Adjustments are made so that the polarization of the two waves becomes orthogonal. In addition to this there is a delay loop in one of the arms such that the two waves become non-overlapping. The phase modulator in the other arm codes the bit value into a phase shift. The light in the fiber after the first interferometer of fig. 2.1 at point (A) is described by the Jones vector.

$$J_1 = \begin{bmatrix} u_1(t)e^{-j\phi_A} \\ u_1(t+\tau) \end{bmatrix} \tag{2.1}$$

This fiber is not polarizing preserving. Despite this, the polarization is preserved due to the orthogonality of the states. In front of Bobs interferometer at (B) a polarization controller regains control of the states of polarization and turns it by $\frac{\pi}{2}$.This process is described by the Jones matrix T_1.

$$\begin{aligned} u_2(t) &= T_1 \cdot J_1 && (2.2) \\ &= \begin{bmatrix} 0 & -1 \\ 1 & 0 \end{bmatrix} \cdot \begin{bmatrix} u_1(t)e^{-j\phi_A} \\ u_1(t+\tau) \end{bmatrix} \\ &= \begin{bmatrix} -u_1(t+\tau) \\ u_1(t)e^{-j\phi_A} \end{bmatrix} && (2.3) \end{aligned}$$

A polarization splitter divides the two states into the two arms. The light was turned by $\frac{\pi}{2}$ in the polarization controller. This means the waves now travelling through the phase modulator in the first interferometer will travel through the delay loop in the second, and vice versa. Without controlling the polarization 50% of the photons would not carry any information. Again, one arm is equipped with a delay loop. The other have a phase modulator

and a polarization controller. Interference requires equal polarization. At the output of the interferometer there is a device, black box, that decides in which arm of the interferometer the photon interferes. T_2 is the effect of the polarization controller and T_3 is of the interferometer. The wave in one of these arms is then described by

$$\begin{aligned} u_3(t) &= T_2 \cdot T_3 \cdot u_2 \qquad (2.4) \\ &= \begin{bmatrix} 1 & 1 \\ 0 & 0 \end{bmatrix} \cdot \begin{bmatrix} -e^{-j\phi_B} & 0 \\ 0 & e^{-j\tau} \end{bmatrix} \cdot \begin{bmatrix} -u_1(t+\tau) \\ u_1(t)e^{-j\phi_A} \end{bmatrix} \\ u_3(t) &= \begin{bmatrix} u(t+\tau)e^{-j\phi_B} + u(t+\tau)e^{-j\phi_A} \\ 0 \end{bmatrix} \qquad (2.5) \end{aligned}$$

This device at (C), according to the assigned bit value, passes the wave through a delay $\widehat{T} = T$ for a '1' or directly $\widehat{T} = 0$ for a '0'.

$$\begin{aligned} u_4 &= T_4 \cdot u_3 \\ &= \begin{bmatrix} 1 & e^{-j\widehat{T}} \\ 0 & 0 \end{bmatrix} \cdot \begin{bmatrix} u(t+\tau)\left[e^{-j\phi_B} + e^{-j\phi_A}\right] \\ 0 \end{bmatrix} \qquad (2.6) \end{aligned}$$

The envelope for the waves at the output of the multiplexer/input of the APD

$$\begin{aligned} u_3^0(t) &= u_1(t+\tau)\left[e^{-j\phi_A} + e^{-j\phi_B}\right] \qquad (2.7) \\ u_3^1(t) &= u_1(t+\tau+T)\left[e^{-j\phi_A} + e^{-j\phi_B}\right] \qquad (2.8) \end{aligned}$$

Distribution of intensity for $u_3(t)$ is given by

$$I = |u_3(t)|^2 \qquad (2.9)$$

This gives two pulses shown in fig. 2.2 that are separated in time. The pulse at $U(t+\tau)$ represent a '0' while $U(t+\tau+T)$ represent a '1'. However, the two pulses is (of course) not both present inside the same gate.An important discovery is that we only need to detect a photon to deside the bit value. Hence, the detector has to be gated at $U(t+\tau)$ or $U(t+\tau+T)$ during a bit cycle.

Classical and quantum domain

The analysis of the interferometer is made in terms of CW-light. This is valid, and the intensity distributions translates into the quantum domain as

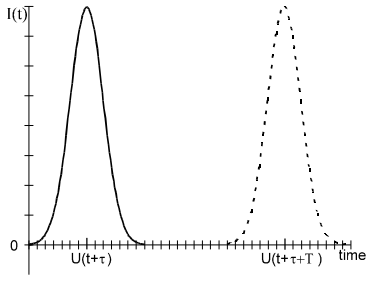

Figure 2.2: Intensity(probability) distribution for interference at time t.

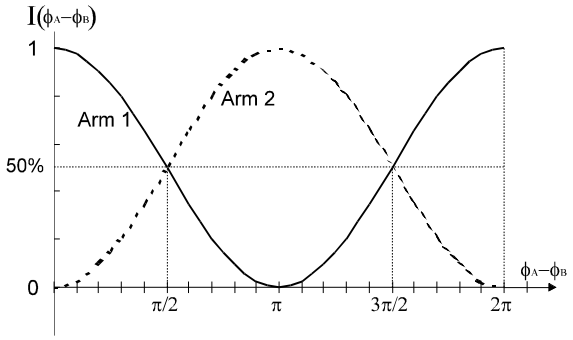

Figure 2.3: Characteristic of interferometer as a function of phase difference in the two arms.

probability distributions. In fig. 2.2 the two bell shaped forms only tells the probability of a photon interfering at a given time. The characteristic of the interferometer in fig. 2.3 tells the probability of interference. Under ideal conditions when the intensity is above the 50% mark there is a probability of one for interfenence. Below the probability is zero.

2.2.4 Keys

The characteristic of the interferometer is the essence in QC. If wrong basis for the measurement is used, that is when $(\varphi_A - \varphi_B) \in \{\pi/2,\ 3\pi/2\}$, there is a probability of 50% whether the measurement is right or wrong. The idea is to employ single photons as carriers of the information. The existence of conjugate observables that are incompatible in the sense that measurement of one necessarily randomized the value of the other[1]. This property does not exist in the classical domain, since classical information i unchanged by the act of measurement. The four basis of phase shifts ϕ used are X–basis

45^o, $+135^o$ and Y-basis $+45^o$, -135^o.

Alice and Bob are sending and measuring at random basis. In 50% of the instances they will have bases that correspond. A measurement will then be correct. The basis information can be exchanged publicly, but the measured value is kept secret. When using same basis they both should have the same bit value, unknown to the rest of the world. An eavesdropper can listen to the quantum channel by beamsplitting. If there is only one photon per pulse she will introduce an error to the system that can only be explained by somebody tampering with the photons. This is the beauty of QC. If the pulse should consist of more that one photon the eavesdropper can make several measurements using different basis' and still leave some photons unchanged for Alice and Bob. Then it's just to pick the measurement that have the correct basis and its corresponding bit value. If this happens QC has failed.

2.2.5 Protocols and QC

Actually how quantum cryptation is done in detail and its protocols are excluded from this thesis. It does not contribute any more to the understanding of how the APD must be operated and the matter of single photon detection. Interested readers are encouraged to read the following sources:

Marand and Townsend, 1997, ref:[1]

Townsend and Phoenix, 1997, ref:[2]

Bennett, 1992, ref:[3]

Chapter 3

Avalanche photo diode

The development of the APD has made it possible to perform single photon detection(SPD) in the near-IR range. However, the theory covering these detectors are mostly concerning macroscopic properties which is adequate, and well developed, for normal operation only. Detection of single photons makes it necessary to consider microscopic properties.

3.1 Single photon detectors

Single photon detection has been preformed with various detectors throughout the visible range and up to near-IR. The detectors however perform differently. Due to physical properties most detectors are only efficient in a limited wavelength window. Fig. 3.1 shows quantum efficiencies obtained for different detectors. For instance, the quantum efficiency(QE) of the InGaAs-APD in the visible light range is very low due to the bandgap. A PMT inside the near-IR the QE has fallen by almost one decade compared to visible light

Most optical networks today are operating at either 1300nm or 1500nm. This is also the reason why effort is put into developing SPD's in the near-IR range.

3.2 Basic theory

3.2.1 APD operation

The basic feature with the APD is the internal amplification. In QC it's exactly that feature that makes it highly usable. Only one incident photon can actually cause an avalanche breakdown. Under ideal conditions almost every incident photon is absorbed, creating a electron-hole pair. Both carriers are

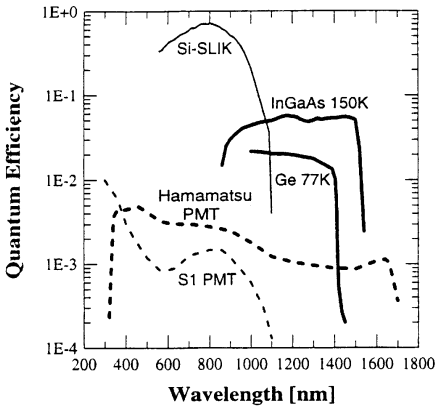

Figure 3.1: Quantum efficiencies of various detectors

accelerated under the influence of a strong electrical field. Upon acceleration the carriers continuously collide with the lattice structure. The typical value of the E-field in the multiplication region of the APD is $\approx 10^5 V/cm$[4]. This soon saturates the velocity of the carriers giving them enough kinetic energy to impact ionize the lattice. More carriers will in order perform the same operation as it's parent carriers.

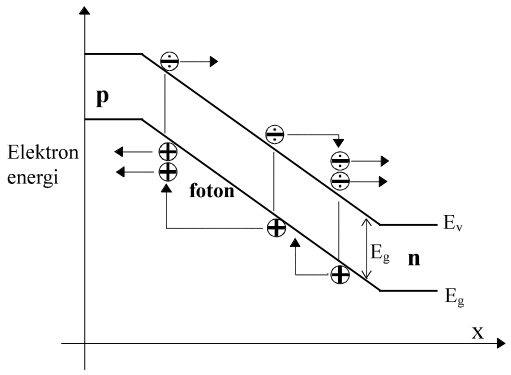

Figure 3.2: Multiplication process of an APD

The multiplication process for both electrons and holes are shown in fig. 3.2

Between the P+ and N- regions in fig. 3.3 there are two separate regions: a lightly doped, low field region(where photons are absorbed and carriers drift according to their polarity) and a heavily doped, hi-field region where carriers undergo acceleration and multiplication. The e-field profile of such

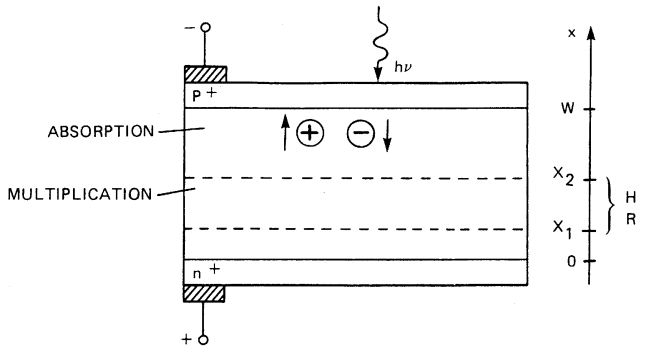

Figure 3.3: A generic structure of an APD.

a structure is shown in fig. 3.4.

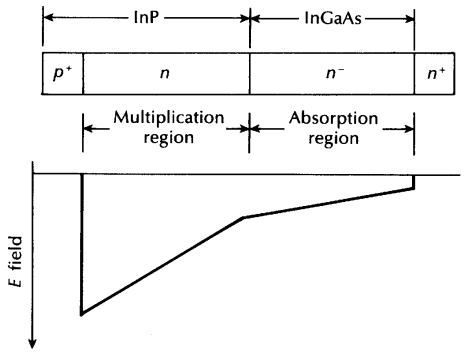

Figure 3.4: The e-field profile through an APD structure.

3.2.2 Design

The APD has a somewhat sophisticated structure. The different regions in fig. 3.3 can differ in composition, type and level of doping. For the QC-project the two types of APD's can be consided, Germanium or InGaAs. Since Ge-APDs traditionally have a higher dark current, the InGaAs is choosen to be the first to be examined. As fig. 3.1 show the Si APD is useless for wavelengths $> 1\mu m$.

The geometry of the APD should maximize the photon absorption, for example by assuming a p-i-n structure. On the other hand the multiplication region should be as thin as possible to prevent uncontrolled avalanches caused by the strong electrical field. These competing requirements are solved by

a *separate absorption multiplication (SAM)* APD[5] structure. That is, the photogeneration of carriers take place in a material optimized for absorption rather that inside the multiplication region. The Germanium and InGaAs APD's are implemented differently, though both support the SAM-mode[1]. Structures realizing these APD's are shown in fig. 3.5

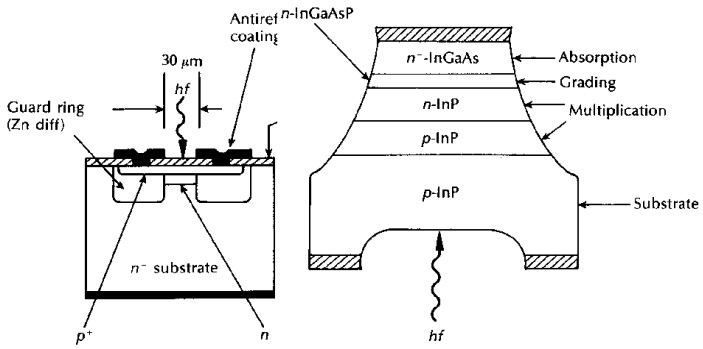

Figure 3.5: Doping profiles of a Ge-APD and a InGaAs-APD.

3.3 Characteristics of operation

In order to utilize the features of the APD it must be connected to proper circuitry. These circuits set the operational characteristics. Empirically the method yielding best results is running the APD in Geiger mode.

3.3.1 Basic circuitry

The basic circuit configuration for the APD is shown in fig. 3.6. The APD is reverse biased V_R, and the signal is read out over a resistive load and amplified. Using the pulsegenerator the bias can be further increased for a short duration of time. This is called Geiger mode(GM) operation.

3.3.2 Geiger mode operation

GM operation is one of the basics in QC when utilizing an avalanche photo diode(APD). It increases the detector efficiency significantly and makes it

[1]Ge APD's with a Hi-Lo structure, featuring low darkcurrents resembles R(each through)-APD structure.[4]. The penetration depth of light into Ge causes separate absorbtion and multiplication. Hence SAM-APD operation.

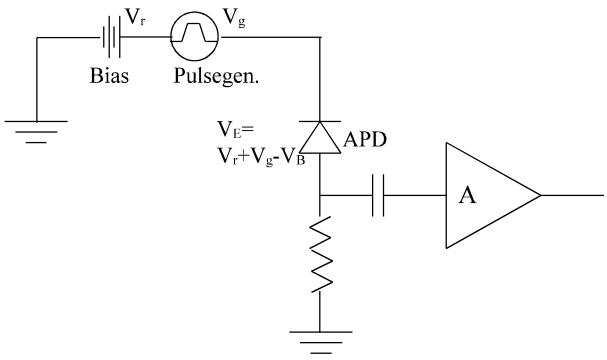

Figure 3.6: Circuitry of Geiger mode operation.

possible to use commercially available APD's. There are a number of parameters related to the Geiger mode

Description

The general idea is to temporarily displace the electrical equilibrium inside the APD. This is done by placing the APD in a gated regime called Geiger mode. For a short period of time the bias is raised above the breakdown voltage. Fig. 3.7 shows parameters characterizing the Geiger operation. Rising and falling times of the edges are neglected and are made as fast as possible. Detection of the single photon is done inside this gate window.

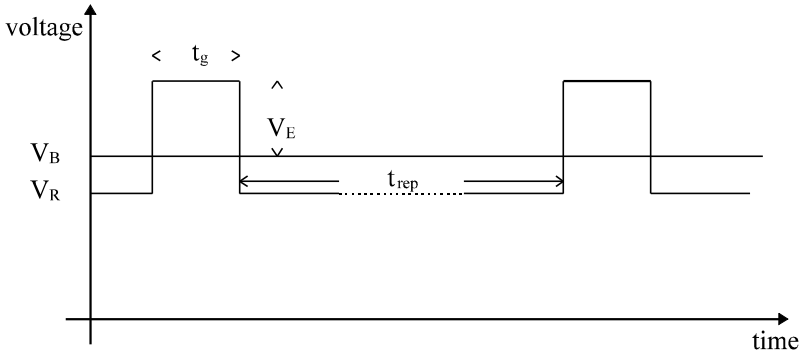

Figure 3.7: Voltage- and time parameters.

Parameters

These parameters describe the basic GM operation. Throughout the whole report they will be used consistently.

V_R	The reverse bias of the APD.
V_B	Breakdown voltage of the APD.
V_E	Excess voltage above V_B from the gatepulse.
V_g	Amplitude of the gatepulse.
t_g	Width of the gatepulse, detection window.
t_{rep}	$\frac{1}{f_{rep}}$ =frequency of gatepulse.

3.4 Physics of operation

When the APD is put into operational mode namely reverse bias and cooling, lots of changes happens. As shown in fig. 3.3 the ADP has a sophisticated doping profile. However, much of the behavior can be explained in terms of a simple pin-junction. Some differences do of course apply and will be accounted for. Reverse bias will from here be referred to as bias since forward bias in not an issue.

3.4.1 Dark current

A major noise parameter in an APD is the dark current. Even though no light is present some current will still flow between the terminals of the device. The magnitude of this current differs, dependent on fabrication. Dark current arises from random electron-hole pair generated thermally or by tunneling. A dark current generated electron will have the same effects as a photogenerated one, thereby multiplication. Tunneling is mostly a matter of design and choice of materials. It is therefore not a process the user can alter by some means of external stress, unless compromising vital properties like bias. However, the thermally generated carriers can obviously be controlled by the temperature. The rate of thermally generated carriers in an intrisic material[6] is given by

$$g(T) = \alpha_r n_i^2(T) \tag{3.1}$$

Where α_r is constant of proportionality and,

$$n_i(T) = 2\left(\frac{2\pi kT}{h^2}\right)^{3/2}(m_n^* m_p^*)^{3/4} e^{-E_g/2kT} \tag{3.2}$$

Hence $g(T)$ exhibits a dependency, decreasing with less temperature and vise versa. By reducing the temperature the dark current can be decreased significantly. The dark current in an APD can be given by

$$I = \frac{dQ}{dt} \tag{3.3}$$

$$\Downarrow$$

$$= \frac{nq}{\Delta t} \tag{3.4}$$

Where q is the electronic charge$(1,6 \cdot 10^{-19}C)$, n is number of electrons and Δt is a time interval, with a convenient scale of ns. The number of electrons passing a cross section per. ns is

$$n = \frac{I \cdot \Delta t}{q} \tag{3.5}$$
$$= 6.26 \cdot 10^9 \cdot I$$

In order to achieve less than one electron per. ns the dark current must be in the sub-nanoampere range.

3.4.2 Electrostatic potential barrier

The *electrostatic potential barrier* is raised when increasing V_R and the difference from the P^+- to N^+-side will be $V_0 + V_R$ volts. This is due to the separation of the energy bands which is a direct function of the electrostatic potential barrier at the junction. V_0 is called the contact potential. The contact potential that appears across the transition region is a built in potential. It is necessary to maintain the equilibrium at the junction, and does not imply any external potential[6].

3.4.3 Electric field

The *electric field* within the APD is a function of the electrostatic potential barrier. The relation is given by Poisson's equation deriving the relation $E(x) = -\frac{dV(x)}{dx}$. As stated, the region between the P^+- to N^+-side has a light doping. Because of this the e-field is not linear through the whole structure, but rather as in fig. 3.4. Hence, it's the doping profile that define the width and the magnitude of the absorption and multiplication regions. It is under influence of the e-field the carriers are accelerated. The simple force relations on a carrier in one dimension yields

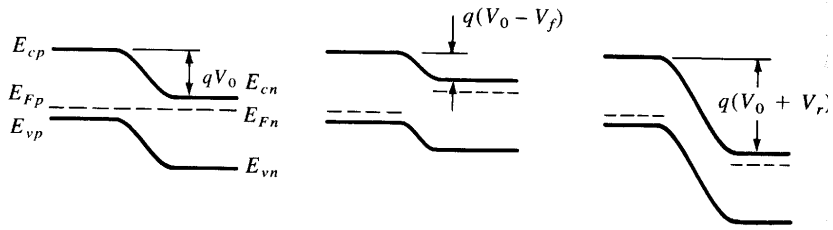

Figure 3.8: The eletrical potensial barrier when in equlibrium, forward bias and reverse bias.

$$F_x = m^* \cdot a_x \tag{3.6}$$

$$F_x = q \cdot E_x \tag{3.7}$$

$$\Downarrow$$

$$a_x = \frac{q \cdot E_x}{m^*} \tag{3.8}$$

The ionization coefficients increase with the depletion region e-field, since it provides the acceleration[5]. A large acceleration increases the mean velocity of the carriers and the probability of ionization with impact. The ionization coefficients α_e and α_h describe the rate of ionization per unit length; the inverse coefficients $\frac{1}{\alpha_e}$ and $\frac{1}{\alpha_h}$ represent the average distance between consecutive ionizations. The ionization ratio is given by

$$\kappa = \frac{\alpha_h}{\alpha_e} \tag{3.9}$$

Single carrier case is achieved when $\kappa = 0$(electrons) or $\kappa = \infty$(holes).

3.4.4 Transition region width

An increasing reverse bias widens the depletion region. The maximum width is given by the distance between the P^+- and N^+ dopings. Beyond this the bias has neligible effect[7]. A very important property is the reach through voltage which is defined by the bias at this point.

3.4.5 Junction capacitance

The transition region exhibits a capacitance. Basically two types of capacitance are associated with a junction, (1) the *junction capacitance* and (2) the

charge storage capacitance. (2) is dominant under forward bias so the major contribution is from (1)[6]. The parallel plate model yields for a junction

$$C_j = \frac{\epsilon A}{W(V_{bias})} \tag{3.10}$$

A typical plot of capacitance vs. bias is shown in fig. 3.9.

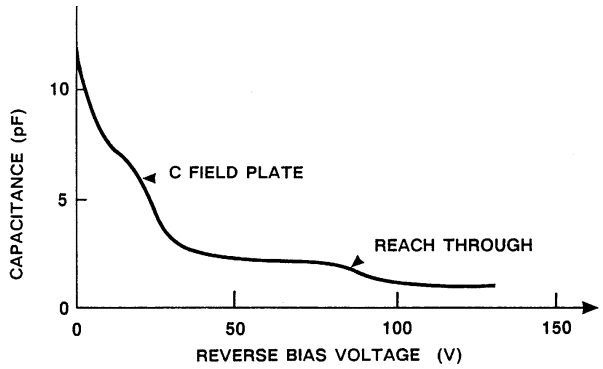

Figure 3.9: Depletion region capacitance as a function of bias.

The unsmooth course of the curve is due to the light doping in the i-region of our "pin-model". It's interesting to observe the lower boundary of capacitance the maximum transition region width defines[7](no exponential decay towards zero).

3.4.6 Reach through voltage

In order to achieve full performance of the APD the bias must be equal or above the reach-through voltage. This important property is dependent only on the doping profiles of the junction[8]. A fast APD is dependent on fast transportation of carriers between the terminals. The terminals can be regarded as either the two ohmic terminals or two strongly doped regions at both sides.

The two mechanisms providing carrier transport are diffusion and drift. Diffusion is not desirable since it's several times in magnitude slower than drift. Drift is identified by an electric field. In order to establish this field the APD-structure must be depleted between the terminals.

3.4.7 Breakdown voltage

By increasing the bias breakdown voltage(V_B) will ultimately by reached. Above this limit the gain is infinite and an unlimited current will flow though the APD, probably exceeding the absolute maximum ratings. If not by some means controlled. The breakdown voltage is defined at the point where the internal gain $G \rightarrow \infty$. The probability that a carrier ionizates the lattice at this point is one. Normal operation is therefore below V_B, yielding a limited gain. Above V_B dark current carriers will instantly be picked up by the e-field and transported to the multiplication region.

In order to achieve breakdown carriers must be present in the depletion region. If not, it would be possible to operate the APD above V_B simply because there had been noting to multiply. Hence, no avalanche breakdown. However the APD is infested with inevitable dark current carriers. The GM avoids this by operating the APD above V_B in such a short period of time that the probability of a dark current carrier being multiplied is small and that an avalanche is quenched before the APD breaks.

This concludes that the bias V_R must satisfy the condition $V_{RT} < V_R < V_B$.

3.4.8 Temperature

The major reason why lowering the temperature to about 77K is the reduction of the dark current. This drastic and somewhat violent action is inevitable in order to conduct the experiments. However, the reduction of dark current is not the only thing that happen. Most of the already mentioned properties is also altered.

Dark current

In chap. 3.4.1 the reduction of dark current vs. less temperature is made probable. Cooling is the key to the success of GM operation. By placing the APD in a cryostat of LN_2(at 77K) the number of carriers is reduced. The APD can by operated above V_B in a gated regime without an avalanche at every gate pulse.

Breakdown voltage

The fact that V_B decreases when temperature is lowered can be explained in terms of carrier scattering. There are two basic types of scattering, impurity and lattice[6]. Fig. 3.10 shows the dependency between the mobility constant μ and temperature.

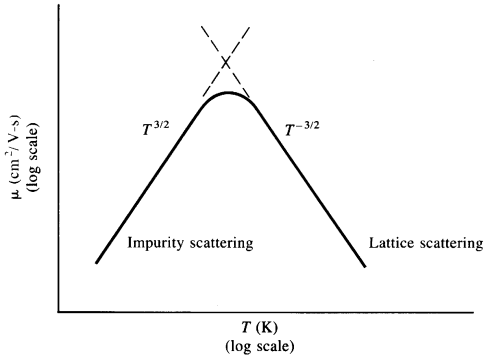

Figure 3.10: Mobility as a function of temperature.

The different contributions of scattering adds inversely up to the mobility μ

$$\frac{1}{\mu} = \frac{1}{\mu_{lattice}} + \frac{1}{\mu_{impurity}} \cdots \tag{3.11}$$

The mobility is increasing with less temperature up to a certain point as in fig. 3.10. This point exceeds beyond our ranges of temperature, so the relation is considered valid down to 77K i.e. lattice vibration is dominant. Electrons and holes have different effective masses m^*. Due to this the mobility μ will have different values for μ_e and μ_h. Despite this is not important to account for in order to state the point. Then, relating the mobility μ to the mean velocity $< v_x >$ in one dimension.

$$< v_x >= -\mu \cdot E_x \tag{3.12}$$

Where E_x has a profile like that of fig. 3.4. Adding up all this concludes that reducing the temperature increases the mean velocity of the photo or thermally generated carriers. The physics behind this is the thermal vibrations in the lattice, reducing the mean free path of the carriers. The larger vibrations the less mean free path. The carriers being accelerated by the field will then be exposed to nonionizating impacts, reducing the kinetic energy. Hence, ionization coefficients are also function of temperature.

Absorption coefficient

One would expect that the absorption coefficient would increase caused by decreasing temperature. When lowering the temperature the Fermi-distribution

becomes a steep function around the Fermi level E_F. A direct result of absence of electrons in the conduction band this is that the available states increases. Thus making an sucessfu ll absorption more probable.

Ionization coefficients

One would also here expect something to happen. As mentioned in sec. 3.4.8 the mean free path increases. Digging into this matter, and two things are realized. The mean free path increases causing the carriers to accelerate a longer distance before colliding. Hence, a larger kinetic energy makes ionization more probable. An ionization is dependent, indeed, on a direct impact with the lattice. The main reason why mean free path increases is that thermal vibrations decreases. The collision cross section is therefore expected to decrease.

$$p_{ionization} = \frac{< v_x >}{V} \cdot \sigma(T) \tag{3.13}$$

The overall effect of temperature on ionization coefficients is therefore a joint function. It is somewhat difficult to say which effect having most weight, larger kinetic energy or less transition cross section.

3.4.9 Trapping

In the energy band profile of the APD there is a discontinuity caused by a heterojunction. Fig. 3.11 visualizes this.

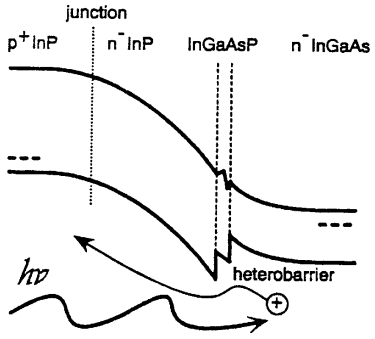

Figure 3.11: Heterobarrier causing trapping of holes in junction.

In conduction band this discontinuity has little or none influence. However, in the valence band holes are trapped. This causes problems. Holes

passing tend to pile up in the heterobarrier instead of drifting to the terminals of the APD. When the V_B is exceeded bt the gate pulse the trapped carriers almost instantly multiply and cause a dark count.

The process of trapping occurs when the APD is conducting. It is then holes are passing the region making trapping probable. When the APD is conducting the current through a cross section is.

$$\begin{aligned} & I_{on} = \frac{dQ}{dt} \\ \Downarrow & \\ n_h \quad = \quad & \frac{I_{on} \cdot \Delta t}{q} \end{aligned}$$

Where the typical $\Delta t = 5ns$. Lets assume that the probability of trapping one hole is p_{trap}. The probability of accumulation of some charge Q_{trap} is then given by a the total number of holes passing the heterojunction n_h, and the probability p_{trap}. A simple model, assuming empty states in the trapping region and ignoring higher order effects, is the Poisson distribution. When the rate of trapping is given by $\lambda = n_h \cdot p_{trap} = \frac{I \cdot \Delta t}{q} \cdot p_{trap}$ then

$$P(n_{trap}) = \frac{e^{-\lambda} \cdot \lambda^{n_{trap}}}{(n_{trap})!} \tag{3.14}$$

Since

$$Q_{trap} = q \cdot n_{trap} \tag{3.15}$$

Hence, trapped charge Q_{trap} is proportional with to I_{on}.

The trapping itself is a function of higer order. The probability of an avalanche is dependent on the history of the last gate pulses. A 1. order process take into account the history of the previous gate and the a 2.order the two last and so on. This result in complicated models that not really is needed. It is however important to be avare of these processes.

Chapter 4

Laser

The QC experiment needs a single photon source. However, this is a non existing device and other measures must be taken to provide single photons. An attenuated laser pulse can be used. The output of this source will have a probabilistic distribution based on the shape and the optical power in the pulse. In order to control the output of our single photon source the laser must be characterized using a detector unit. The laser is a Fujitsu FLD3F6CX.

4.1 Detector

To characterize the laser, the detector intended for this, must be characterized itself. The detector consists of several parts; a photodiode, a biasTee and an amplifier. Available data for the devices are enclosed in the appendix.

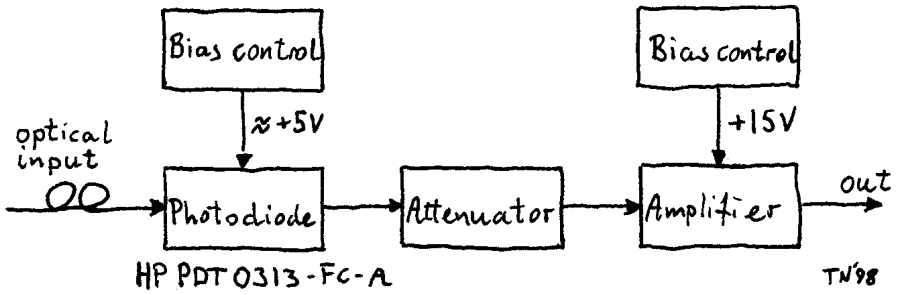

Figure 4.1: The parts constituting the detector unit.

4.1.1 Test mode

We want to check if the experimental and theoretical responsitivity of the system agrees. This is done by applying sine waves of known current amplitude to the laser. By relating the current to the enclosed test characteristics and compare this to the curve shaped by the detector unit we can find the responsitivity.

Circuitry and experimental setup

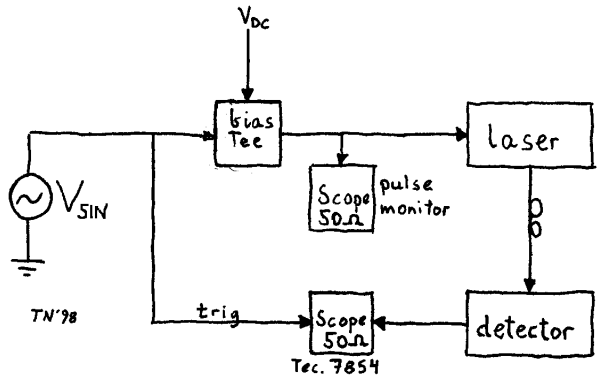

Figure 4.2: Block view of test setup.

The complete block view is shown in fig. 4.2. A function generator provides a sine-wave and the bias is controlled via the biasTee. A scope is monitoring the voltage pulse at the output of the biasTee. The output of the detector is observed on a 15GHz sampling scope.

Inside the laser module there is a 20Ω resistor in series with the laser diode. Close to this resistor there is in addition an external 300Ω resistor as shown if fig. 4.3. This resistor provides a high impedance compared to the laser, and do therefore determine the amplitude of the current. I.e. the laser sees a current source.

Experiment

The gain curve of the amplifier in fig. 4.2 varies by $\pm 2\,dB$. A sine-wave, which makes it simple to determine the gain at a specific frequency is therefore applied. The frequency of the sine is $200MHz$. The voltage is adjusted such that the current pulse is right above the I_{th}. This is observed as oscillations occurring then lowering the bias provided by the DC-source. Reading the

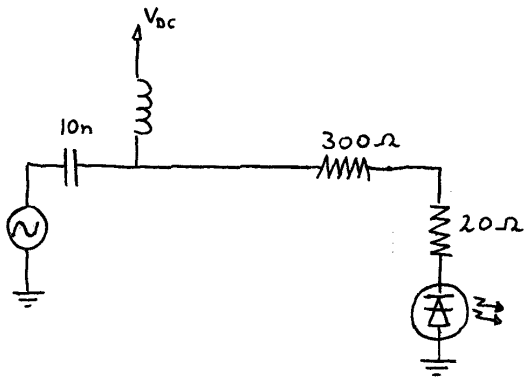

Figure 4.3: Electrical equvivalent of the test circuitry of the laser.

voltages on the monitor scope at this operating point:$V_{DC} = -6V$, $V_{AC} = 4.15V_{p-p}$.

The peak to peak current of the pulses is given by Ohm's law. Compensation for the dynamic resistance of the laser diode 10Ω is included in addition to the 300Ω and 20Ω.

$$\begin{aligned} I_{pulse} &= \frac{V_{monitor\_scope,p-p}}{R_{external} + R_{internal} + R_{dynamic}} \\ &= \frac{V_{monitor\_scope,p-p}}{330\Omega} \end{aligned}$$

This yields

$$\begin{aligned} I_{pulse,MAX} &= \frac{(6 + 2.08)V}{330\Omega} \\ &= 12mA \\ I_{pulse,MIN} &= \frac{(6 - 2.08)V}{330\Omega} \\ &= 24mA \end{aligned}$$

Looking up in the optical power vs. current characteristics of the laser the current pulses correspond to approx. $0.75W_{p-p}$ of optical power. These current pulses results in a sine-wave on the sampling scope, $V_{p-p} = 238mV$. The responsitivity $\Re$ of the system is experimentally determined

$$\begin{aligned} \Re &= \frac{238mV}{0.75mW} \\ &= 317mV/mW \end{aligned}$$

Theoretical calculation

The responsitivity of the system can also be calculated by using figures in the specifications. The typical resonsitivity of the photo diode is $0.75mA/mW$.

$$\begin{array}{c} 0.75mA/mW \\ \Downarrow \\ 37.5mV/mW \ @50\Omega \end{array}$$

The signal propagates through an attenuator of 6dB

$$\begin{array}{c} 6dB \\ \Downarrow \\ 18.79mV/mW \ @50\Omega \end{array}$$

At $200MHz$ the gain of the amplifier is approx. $23dB$.

$$\begin{array}{c} 3dB \\ \Downarrow \\ 265mV/1mW \ @50\Omega \end{array}$$

Responsitivity of the system is theoretically determined $\Re = 265mV/1mW$.

Conclusion

The experimentally determined responsitivities of the system is in good agreement with those calculated theoretically. We will use a coefficient of $\Re = 300mV/mW$ in further calculations. However, the amplifier gain varies by $\pm 2dB$ across its frequency range of $0.1GHz$ to $18GHZ$. Furthermore, when it comes to estimating en energy of a short laser pulse, a safe overall error range would be 50% -100%.

4.2 Single photon mode

4.2.1 Theory

This section is not intended to lecture about lasers but rather to gave a brief understanding of the physics behind the gain switching. Below threshold the

laser operates like a LED. To avoid background noise from this LED effect the laser must be switched from zero bias. This was confirmed experimentally[1]. A short voltage pulse provided by the SRD-unit raises the bias above threshold. This causes a sudden buildup of the photon number density, $P_0(t)$ due to laseing. However, this buildup of photons in the cavity quickly eats the population inversion $N(t)$ and the number of photons decreases quickly. $P_m(t)$ is extremely sensitive to small variations in $N(t)$. The population inversion again starts building up, but before the photons start laseing the bias is turned off. This process in described in fig. 4.4. By isolating one such a optical cycle, marked with an arrow, a very narrow optical pulse can be emitted from the laser.

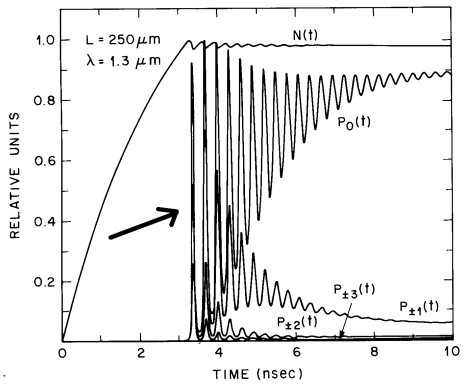

Figure 4.4: Time evolution of the carrier and photon population exhibiting relaxtion oscillations.

4.2.2 Step recovery diode

The circuitry providing the pulse consists of a step recovery diode(SRD)

The components are soldered as close to the modulation terminal of the laser as possible. This prevents ringing due to mismatch and the high frequency signals we are dealing with. The block view is shown i fig. 4.6.

The circuit is relative insensitive to the input pulse width. The amplitude of the pulse can be adjusted with both the bias and the input pulse amplitude.

[1]A simple exeriment was done. Laser was connected to the APD setup and bias was applied. By adjusting the bias higher the counts of the APD increased.

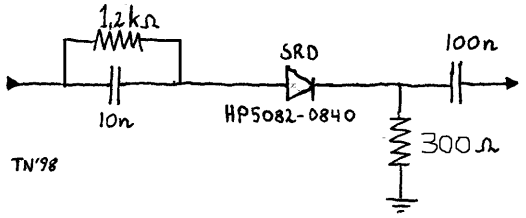

Figure 4.5: Pulsing circuitry using a step recovery diode.

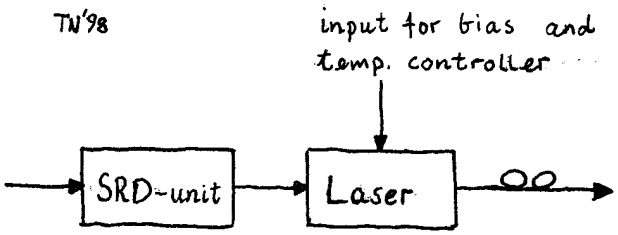

Figure 4.6: The laser in pulsed mode.

4.2.3 Pulse power

Now, as we know the responsitivity of the system it is possible to calculate the energy in the pulse by analyzing the output of the detector. The relation of optical power and voltage on the scope is, assuming that the impulse response of the detectorsystem is much smaller than an optical pulse.

$$\begin{aligned} V_{p-p,scope}(t) &= \Re \cdot P_{optical}(t) \\ &\Downarrow \\ P_{optical}(t) &= \frac{V_{p-p,scope}(t)}{\Re} \end{aligned}$$

and this gives the relation to the energy

$$\begin{aligned} E_{optical} &= \int_{t_1}^{t_2} P_{optical}(\tau)d\tau \\ &= \frac{1}{\Re}\int_{t_1}^{t_2} V_{p-p,scope}(\tau)d\tau \end{aligned}$$

The area that the voltage pulse spans out can be calculated by the *area*-function provided by the oscilloscope.

4.2.4 Pulse efficiency

The energy of the pulse is proportional to the number of photons. The energy of n photons in a pulse is given by

$$\begin{aligned} E_{optical} &= h \cdot \nu \cdot n_{photon} \\ &\Downarrow \\ n_{photon} &= \frac{E_{optical}}{h \cdot \nu} \end{aligned}$$

The pulse with the specified optical energy is passed through an optical attenuator with a loss of D dB. This determines the average number of photons,hereby called the pulse efficiency, of the optical pulse.

$$\eta = \frac{n_{photon}}{10^{D/10}}$$

4.2.5 Statistics of the pulse

Number of photons

The number of photons in the pulse is Poisson distributed. The parameters in the Poisson distribution is given by the pulse efficiency of the attenuated laser pulse. The probability of x photons in a pulse, $P(x)$, is given by

$$P(x) = \frac{e^{-\eta} \cdot \eta^x}{x!}$$

If the pulse efficiency is too large there is a higher probability of more that one photon per. pulse. Values for different η(values omitted (-) since $\gg \eta$ represent insignificant figures of magnitude).

	$\eta = 0.05$	$\eta = 0.1$	$\eta = 0.5$	$\eta = 1$	$\eta = 5$
$P(x = 0)$	0.95	0.905	0.607	0.368	0.0067
$P(x = 1)$	0.048	0.0905	0.303	0.368	0.0337
$P(x = 2)$	1.19m	0.0045	0.076	0.184	0.084
$P(x = 3)$	19.8u	0.15m	0.013	0.061	0.140
$P(x = 4)$	-	3.7u	1.6m	0.015	0.175
$P(x = 5)$	-	-	0.16m	3.1m	0.175
$P(x = 6)$	-	-	-	0.51m	0.146
$P(x = 7)$	-	-	-	-	0.10

(4.1)

An interesting observation is the magnitude of the varians σ^2 when η increases. The varians is given by $\sigma^2 = \eta$. Also, values that is omitted because they r

Jitter

Arrival times of the photons will be distributed according to the shape of the optical pulse of the output of the laser. This causes a phase jitter. The maximum of this jitter is given by the width of the optical pulse. Our pulse is about $100ps$ wide, FWHM, and look like fig. 4.7.

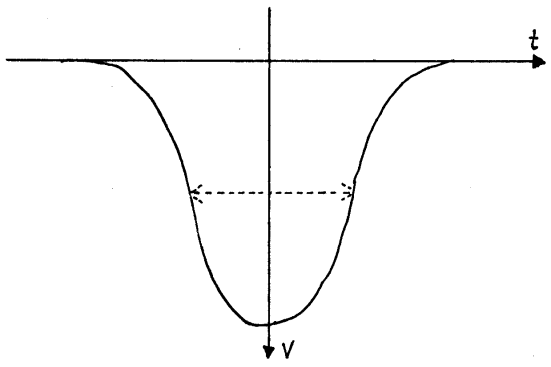

Figure 4.7: The laser pulse detected by the characterization setup and read on the 15MHz scope.

Chapter 5

Models of performance

In order to evaluate the APDs a set of performance measures must be developed. This must be done to identify the optimal characteristics of operation because there is not a obvious way to find this. It's composed by several trade-offs. Now, keeping the physical characteristics from chap3 in mind, this can be related to the performance characteristics.

5.1 Performance measures

Many of the physical properties of the APD are related. Changing one property may often change others as well. To achieve the best possible performance all the operational parameters must be correctly set. However, trying to improve one specific property by adjusting one parameter might not have the desired advantage. An improvement like this often causes a depreciation that cancels the achieved advantage. An example of this can be the QE/dark count matter. Both properties increases when changing the excess voltage. This means that more photons can be detected successfully. But the dark current is subject to same the increased probability of detection. If both properties increase at the same rate no improvement is achieved, the ratio of photo count and dark count rate stays constant. It is though difficult to know in which order two competing properties change. If the good property improves four times and the bad dereciate twice it is safe to say that the adjustment was advantageous.

A set of performance measures, referred to as efficiencies, will bring the matter of all the competing properties into consideration. The efficiencies are concerning the three major properties dark counts, detection performance and the rep.rate(bit rate). The two first are functions of $X \in \{V_E, V_R, t_g\}$ and f_{rep}. The upper boundary of a (dark/photo) count is the rep.rate. The

rep.rate is the maximal number of gates per. second and a count is possible only when the APD is gated. The efficiencies are thought to reflect the portion of disadvantageous/advantageous instances to the rep.rate. The efficiencies $\eta \rightarrow 1$ when subject to optimal conditions.

The object of this section is to establish a more general way of how to evaluate an APD as a SPD.

5.1.1 Dark counts

Dark current counts are possible to measure by simply not coupling light into the fiber. Then, for certain values of X and f_{rep} a dark count rate $\overline{n}_{dark}$ can be detected. The error rate in persent is

$$e(X, f_{rep}) = \frac{\overline{n}_{dark}}{f_{rep}} \cdot 100\%$$

Assuming that a dark count corrupts the information and thereby makes it useless leaves a portion of still potential useful bits.

In order to conduct a complete QC experiment the dark counts must be kept low. Otherwise, the error correction codes[1] will not be able to their jobs. So, it is therefore a very good idea to look at the dark counts before starting any experiment. A qualified guess for the dark count error rate is $e(X, f_{rep}) = 0.005$.

Saying that a dark count makes the bit information useless is somewhat false. The instance where both a photon and a dark current carrier is present at a gate might very well happen. Another instance is when the photon doesn't reach the APD and a dark current carrier causes avalanche. In both examples the information is valid. For now this is a good model since it is desirable to keep the dark counts as low as possible.

5.1.2 Photon detection

A problem arises when single photon is to be counted. There is no way to avoid dark counts which will, as well as the photo counts, contribute to the total number of counts. Also, the laser light source cannot deterministically emit only one photon per pulse. The number of photons in a pulse is described by statistics, making it even a little more complicated.

[1] This is however a matter for somebody else to implement. They will also set the limit of how many errors the codes can handle.

Photons

The laser can have a photon(pulse) efficiency $\eta_{photon} = 0.5$, meaning 5 photons per 10 pulses. Probabilities using Poisson distribution is listed in table 4.1. The rate of photons sent is

$$\overline{n}_{sent} = \eta_{photon} \cdot f_{rep} \tag{5.1}$$

Detection

Since the detector is supposed to detect single photons the photon efficiency of the laser must be kept > 1. If not, there is a too high probability that more that one photon is emitted in a pulse. This in term makes it impossible to determine the exactly when a photon arrives. The efficiency of detection must therefore be based on the differential figure of detected counts and dark counts. The rate of dark counts $\overline{n}_{dark}$ must be determined in under identical conditions as for the detection trial. Since there is less that one photon per pulse the rate of detected photons is given by

$$\begin{aligned} \bar{n}_{photons} &= \frac{\bar{n}_{detected}}{\eta_{photon}} - \bar{n}_{dark} \\ &= \frac{\bar{n}_{detected} - \eta_{photon} \cdot \bar{n}_{dark}}{\eta_{photon}} \end{aligned}$$

The rate of photons detected are the related to the rep.rate

$$\eta_{deteced}(X, f_{rep}) = \frac{\bar{n}_{photons}}{f_{rep}} \tag{5.2}$$

$$= \frac{\frac{\overline{n}_{detected} - \eta_{photon} \cdot \overline{n}_{dark}}{\eta_{photon}}}{f_{rep}} \tag{5.3}$$

$$= \frac{\overline{n}_{detected} - \eta_{photon} \cdot \overline{n}_{dark}}{\eta_{photon} \cdot f_{rep}} \tag{5.4}$$

The photons will then, if detected, cause $\overline{n}_{detected} > \overline{n}_{dark}$. The magnitude of $\eta_{deteced}$ tells how many of the counts that actually are correct.

The theoretical figure of detector efficiency is embedded into the expression. The detector efficiency η_{QE} is given by

$$\begin{aligned} \eta_{deteced} &= \eta_{QE} \cdot (connectors) \cdot (fiber) \\ &= \eta_{QE} \cdot d_{connector} \cdot d_{fiber} \end{aligned}$$

The η_{QE} is therefore slightly large that what measured.

5.1.3 Repetition rate

Think for a moment that 100% detection efficiency could be achieved by transmitting one bit each hour. The successful bit transmission rate would then not been overwhelming. Rep.rate must therefore be brought into consideration. Error correcting codes allows us some bit errors. The cost of this is some of the transferred bits. In a real life system there will always be a certain error rate. By increasing the rep.rate we might increase the dark counts(this will be accounted for by η_{rep}), but at the same time we will also get more bits successfully transferred.

When the gate is off there is some dead time t_{off} where photons cannot be detected nor sent. This off time is useless in the sense of transmission. The maximum value of f_{rep} is in experiments like these about $f_{max} = 1MHz$. We have that $\frac{1}{f_{rep}} = t_g + t_{off}$. Since $t_g \ll t_{off} \Rightarrow t_{off} = \frac{1}{f_{max}}$. The measure of utilization of time can therefore be written

$$\eta_{rep}(f_{rep}) = \frac{f_{rep}}{f_{max}} \tag{5.5}$$

A low rep.rate f_{rep} utilizes the time poorly. While when $f_{rep} = f_{max}$ the APD is used at its maximum limit. This limit can be set by a high number of darkcounts. To compare several APDs the f_{max} must be set to a fixed value for all trials. Unless this is done it will be impossible to evaluate the processed datas.

The rep.rate problems can be made insignificant by applying an adaptive rep.rate circuitry. It's only when an avalanche has occurred that the APD needs rest due to carrier trapping. Theoretically, in absence of avalanches, the APD can be gated at a rate of magnitude of tens of MHz. This will not be dealt with in this thesis.

5.1.4 Joint functions

The question is how how to determine the performance of an APD. By combining the efficiency models this can be achieved. Since the error rate should not exceed some value of approx. 0.5% the error rate should be presented as a separate curve along a secondary y-axis. This gives a better visualization.

5.2 Physics of performance measures

The listed performance measures are functions of X and $f_{rep.}$ When considering the relations it's realize that there are two *fundamental* properties. The

detector efficiency and dark current counts are the properties that determines the performance. How to control these two properties are answered in this section.

5.2.1 V_E, excess voltage

The excess bias has two apparent effects. Increasing both detector efficiency and dark current counts.

Detector efficiency

The excess bias V_E is proportionally related to the e-field inside the APD. This in terms decide the magnitude of the ionization coefficients. When raising the V_E it is therefore expected that probability of an avalanche is increased. That is when a photogenerated carrier is present. V_E is therefore preferred as high as possible in order to achieve the best QE for the APD as possible.

Dark current

V_E is expected to increase dark current counts. It will not alter the rate of thermally generated carriers. By increasing the V_E the ionization coefficients increases and thereby also the dark current counts. These carriers are subject to the same increased probabilities for avalanche as the photogenerated ones.

5.2.2 V_R, bias

V_R sets the magnitude of e-field when gate is off. It is therefore the parameter that sets the operational characteristic when the APD is off.

Breakdown

The bias V_R must be operated below breakdown V_B. Above V_B the dark current will multiply. A saturated current will continuously flow through the APD according to magnitude of the bias.

Reach through

In order to obtain optimal efficiency the APD must be fully depleted. This is achieved when V_R exceeds V_{RT}.

Trapping

The bias will have a reducing effect on some of the dark counts. Trapped holes in the heterobarrier is during gat off time swept out of the junction. The extent of this sweeping is somewhat fussy but it is expected that a highest possible V_R right below V_B will sweep the most holes. This is because the largest V_R gives the strongest e-field.

5.2.3 t_g, gate width

Dark current counts

A number of carriers are passing a cross section of the APD due to dark current. The probability of a carrier being present within the gated period is proportionally increased by a larger t_g. This increases probability of an avalanche and thereby a dark current count. Equally, the dark current counts will decrease when t_g is reduced.

Trapping

Trapping occurs when carriers passes the junction. The magnitude of the charge passing a cross section of the junction is given by the length of the gate. An avalanche is only possible during a gate pulse. The avalanche will also last until gate is off. A short gate length will reduce the probability of some trapped charge. The less charge in the barrier the less probability of a dark count at the next gate pulse.

Detector efficiency

A interesting combination is V_E and t_g. To compensate for increased dark current counts when increasing the excess voltage the gate with can be reduced. The overall result is better detector efficiency at a constant dark current count level.

5.2.4 f_{rep}, repetition rate

Trapping

After an avalanche holes are trapped. To prevent dark current counts they have to be swept out. This happens when the gate is off. The off time $t_{off} = \frac{1}{f_{rep}} - t_g$. Since $\frac{1}{f_{rep}} \gg t_g$, $t_{off} \approx \frac{1}{f_{rep}}$. If t_{off} is made to small or f_{rep} too large all the holes are now swept away making an avalanche more likely at

the next gate. Reducing the rep.rate will only improve efficiency of when trapping is the major source of unwanted counts.

Chapter 6

Preliminary measurements

The optimization of operation characteristics includes several parameters. To simplify the analysis an objective should be to reduce the number of parameters. This will save time and effort and most likely not affect the result.

6.1 Experimental setup

The experiment was aimed at the dark count rate and the distribution of avalanches inside the gate for the parameters of $X \in \{V_E, V_R, t_g\}$ and f_{rep}. The purpose of these trials were to verify the already established theory in chap. 3. Another important reason is to relate the parameters to the physical properties.

6.1.1 Circuitry

The circuitry in fig. 6.1 and cryostat used were a temporarily setup designed for the purpose of detecting avalanches and arrival times of avalanches. The circuitry has a high degree of symmetry. The gate pulses causes transients at its edges because of the junction capacitance of the APD. These transients are often higher in amplitude than the actual signal. Detection of a signal is therefore difficult since a transient is present at every gate and the avalanche is not. By simulating the junction of the APD by using a capacitor C_1 the transients can be subtracted, leaving a somewhat clean signal.

Since the arrangements only were made for test purposes, no other specifications were made. The component limiting the bandwidth is the 1 GHz opamps used in the differential stage.

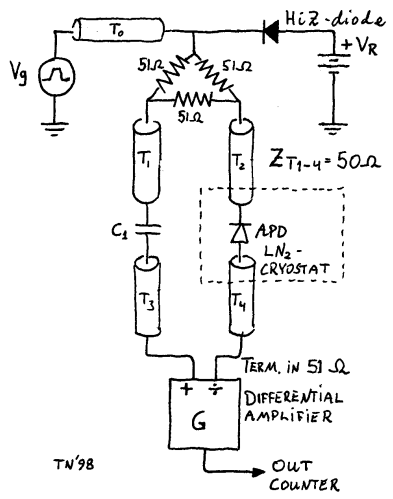

Figure 6.1: Test setup of APD-circuitry and cryostat.

The output of the circuitry was connected to a counter, the Stanford Research SR620.

6.2 Measurements

The measurements were made by using a counter, SR620, witch was connected to the OUT COUNTER at fig.6.1.The *trigger out* at the pulse generator was also connected to the SR620. This simple setup could count the number of avalanches from the APD and make a histogram of the distribution in time of the avalanches. Only plots and key values are presented here. The complete tables are included in the appendix.

6.2.1 Bias

Constraints and plots

Three trial were made, one for each different excess voltage. The operational parameters were:

$t_g = 10ns$

$f_{rep} = 100kHz$

In fig. 6.2 the counts are plotted vs. the bias V_R. It's not so clear for low values of V_E that the bias V_R affects the dark count rate in a beneficial manner. The slope of the curve for $V_E = \{1.0, 1.5\}$ is small and almost flat

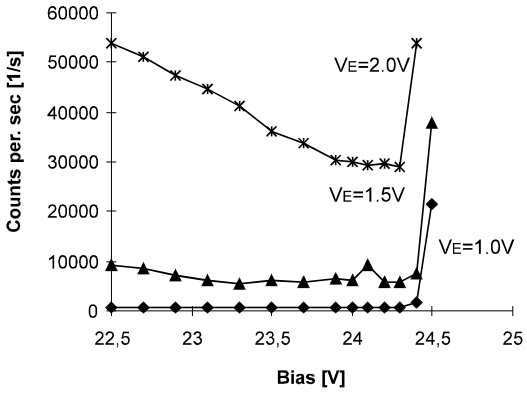

Figure 6.2: Dark current counts vs. bias.

until breakdown V_B is reached. Hardly any carriers are trapped or multiplied at these excess voltages.

At the highest excess voltage $V_E = 2.0V$ the counts decreases when increasing the V_R before reaching V_B (this is also feebly suggested in the beginning of the $V_E = 1.5V$-curve.) From $22.5V$ to $24.3V$ the dark counts per second falls by 20000/s.

Conclusion

For low values of V_E the bias does not affect the dark count rate. At higher values of V_E the bias should be placed as close to the V_B as possible. This minimizes the dark current count rate due to trapping as predicted in the APD-theory chapter. By doing so carriers are driven successfully out of the junction. Hence, V_R could be placed close to the V_B for all values of V_E. This value of V_R must be experimental determined. In our trials a good estimate is $V_B = 24.3V$.

6.2.2 Gate width

Constraints and plots

The operational parameter were:

$V_E = 1.5V$

$V_R = 23.7V$

$f_{rep} = \{100, 500\}\, kHz$

The plot in fig. 6.3 is a plot of the unprocessed collected data. More interesting is a look at the number of counts per ns of a specific gatelength. The data in fig. 6.4 is counts divided on its corresponding gatelength.

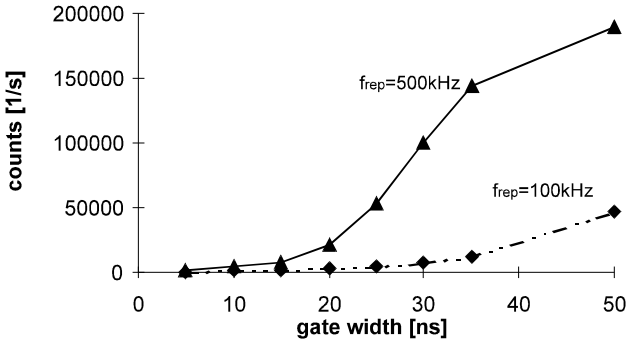

Figure 6.3: Dark current counts vs. gate width.

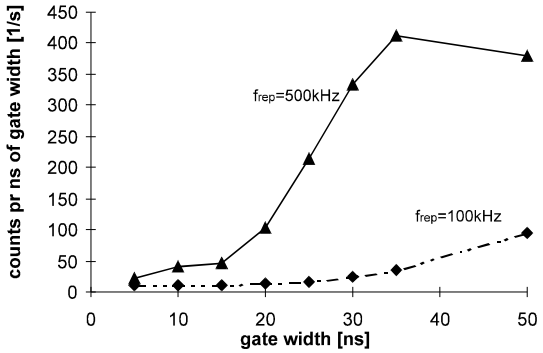

Figure 6.4: Dark current counts per. ns of gate width.

For the $f_{rep} = 100kHz$ curve there is a independence on counts per. ns of gatewidth up to $t_g = 30ns$. The other curve $f_{rep=}500kHz$ the independence is only valid to about $t_g = 15ns$. Above this the counts rise sharply.

Conclusions

The source of dark count in the $100kHz$-curve is mainly thermally generated carriers. The mean number of counts should then be linear with the gate length. Trapping is probably the cause of the sharp rising slope of the $500kHz$-curve. A fast repeating gate pulse combined with a long gate width increase the probability for trapping.

However it is concluded in the opening chapters that we only need to **detect** an avalanche. Discrimination of arrival times is not necessary. Therefore the gate width should be kept as narrow as possible. The lower boundary of the gate width is limited by the response time of the APD and the amplifier

circuitry. The bandwidth of the APD is $2.5GHz$ and $1GHz$ for the opamp.

6.2.3 Rep.rate

Constraints and plots

The operational parameter were:
$V_E = 1.5V$
$V_R = 23.7V$
$t_g = \{10, 20\}ns$

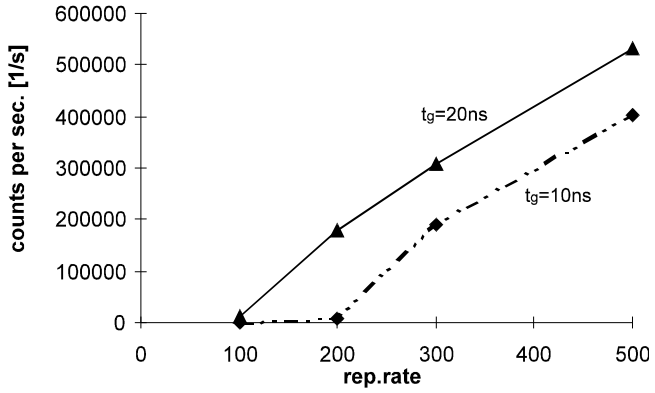

Figure 6.5: Dark current counts vs. rep.rate.

Dark counts in fig.6.5 for the $20ns$ gate rises immediately when increasing the rep.rate. The $10ns$ gate counts is also rising but this does not happen until a rep.rate of $200kHz$ is reached. Before that the count rate is almost unchanged

Conclusions

The rep.rate is limited by trapping, but is also influenced by the gate length. Gate pulses of $10ns$ can be run at rep.rates of $200kHz$ before experiencing the same rise in counts as the gate pulses of $20ns$ at $100kHz$. It looks a too long gate width causes a higher probability of trapping charges. If the rep.rate is too large all the carriers will not have time drift out of the junction. It is therefore expected that by reducing the gate width the rep.rate can be increased. This can be done to a certain point without resulting in increased trapped carrier counts. The counts caused by dark current carriers will still be the same and will be a lower boundary of undesired counts.

6.3 Histograms

Histograms were plotted for several settings. However, many of the plots seemed to not make any sense. Even if the gate width was 10ns the histogram showed 20ns. Both figures should be in about the same order. Jitter could of course explain some deviation but not as much as 100%. The most probable explanation is the act of measurement. Luckily did this not affect the counts.

Some of the plots seemed correct and they support the established theory. When trapping started to be significant the arrival of counts started to gather around the start of the gate pulse. The distribution of avalanches were exponential-like.

Chapter 7

Circuitry and settings

The circuits, laser, power supplies are mounted into a standard Vero frame. This will probably make it more easy for other users than the constructor. The different parts are mounted into modules that are easy to replace and remove for modification or service.

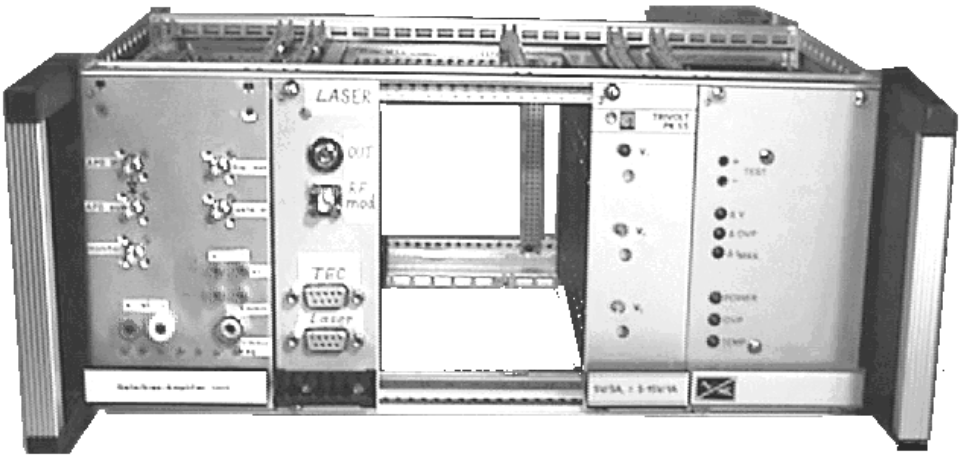

Figure 7.1: The Vero frame where several parts of the experimantal setup is mounted.

Till now there are four pars modules occupying the rack. The power supply#1 is not in use and not connected to anything. It's thought to provide the bias to the APD when characterization and experimenting is done. Now, the bias is provided by an external power supply. The modules have the following slot designations

Module	Slot number
Powersupply #1	47
Powersupply #2	39
Laser	31
APD circuitry	1

7.1 APD circuitry

7.1.1 Technical data

The APD is cooled so most of the characteristics is changed. The key data we're interested in are the breakdown voltages. These are

Temperature	V_B
-198°C	24.1
-188°C	24.7

The breakdown voltages are determined by a little experiment. The anode of the APD is disconnected from the circuitry and a 1MΩ resistor is connected to the ground. A scope of 1MΩ input resistance measures can measure the current. By increasing the bias(no gate pulse present) the "knee" of the avalanche(IV-curve) is observed on the scope. The value V_B might not be chosen at the value corresponding to definition of breakdown. Anyway, it close enough and at the "knee" the APD already has an significant amplification.

7.1.2 Mounting

The APD circuitry is mounted into a standard Vero module. The power is supplied through the connector in the rear and regulated by some common used voltage regulators. The pin designations are

Rear pin	Input [V]	Regulator	Regulated [V]	Designation
4a	+15	7805	+5	opamp
4c	-15	7905	-5	opamp
6a	+15	LM319	5-10	mmic
2a/c	Ground	-	-	-

The regulators are made in agreement with design suggestions supplied in any catalog or data sheet. All inputs are connected to an indicator LED(180Ω) in the front panel. The adjustment pot.meter for the mmic is also located in the front panel.

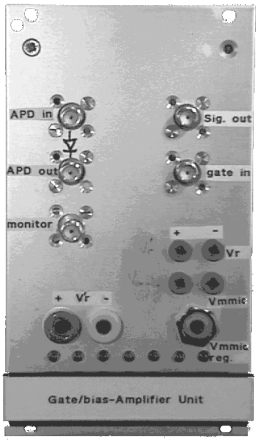

Figure 7.2: The front panel of the APD-circutry module.

7.1.3 Basic configuration

Basics

The basic configuration of the circuits around the APD is shown in fig.7.3. This constitutes the Geiger mode configuration. There is the pulsegenerator of 50Ω output. A 500Ω probe links the biasTee to the connector of the pulsegenerator. The transmission line is split in two by the delta coupler. This provides matching of impedance in all directions. The probe does not contributes to any significant mismatch. The two transmission lines are both terminated in a differential amplifier stage(at the bottom of fig.7.3).

Terminations

Inside the cryostat there are soldered terminations of the 50Ω transmission lines. To block the DC component from the bias there is two capacitors in series with the 51Ω resistors. Two 51Ω resistors behind the APD and the C_{APD} reduces noise(ringing). This is experimentally confirmed.

The components inside the cryostat are not soldered directly together. They are suspended by thin wires so that any thermal stress don't cause any damage. The two lines the connected into a differential amplifier stage.

Differential stage

This circuit cancels the transients caused by the pulsing and the junction capacitance of the APD. From a junction capacitance point of view the APD

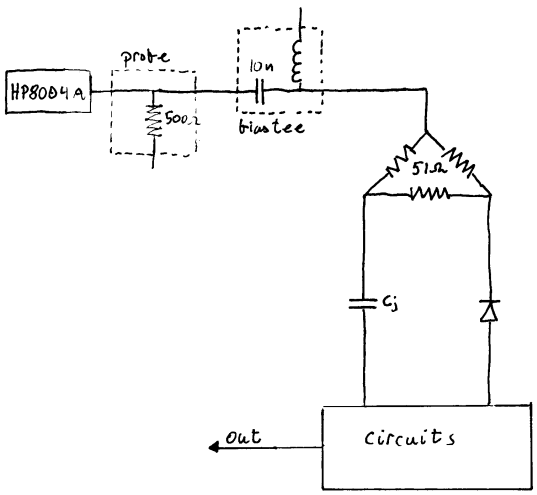

Figure 7.3: The gate and bias configuration of the APD

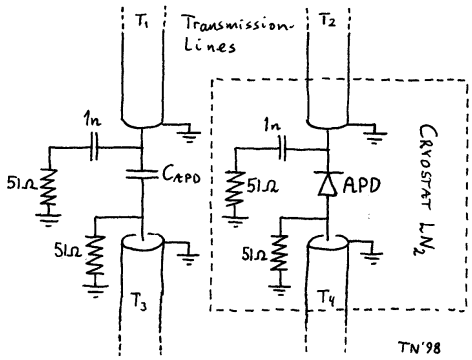

Figure 7.4: Terminations of the transmission lines inside the cryostat.

can be replaced by a capacitor. Simply by applying a high degree of symmetry the transients can removed from the signal by subtraction.

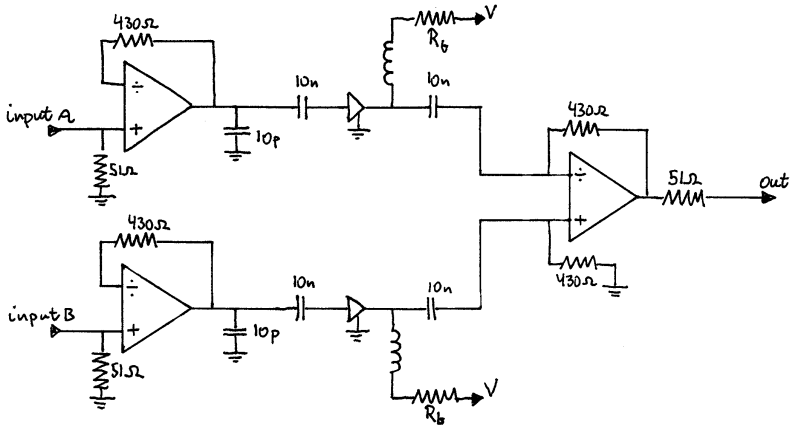

Figure 7.5: The differential amplifier stage with adjustable amplification.

This circuit was the one first made and doesn't comply any design suggestion. Since it works well it's not tampered with. However, an improvement should be made if gate pulses $> 4ns$ will be applied. The frequency response is reduced by the buffer in the input stage and two amplifiers are redundant. One amplifier can be placed at the output.

7.2 Laser

7.2.1 Technical data

The laser is a Fujitsu FLD3F6CX laser. The key figures is

ITEM		CONDITIONS	LIMIT	VALUE	UNIT
Threshold current	I_{th}	CW	4 ~20	8.7	mA
Slope efficiency	S	CW, Pf=2mW	0.05 ~0.083	0.063	W/A
Monitor current	I_m	CW, Pf=2mW	0.1 ~1.0	0.342	mA
Peak wavelength	λ_p	Note [1]	1290 ~1330	1309.3	nm

(7.1)

The bias controller used are the Lightcontrol Instruments INC,MODEL502.

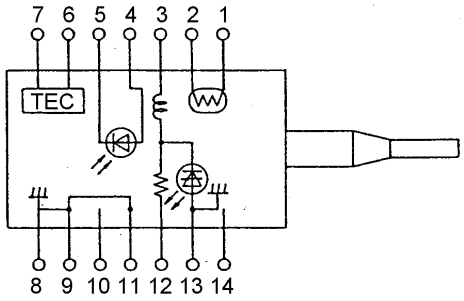

Figure 7.6: Top view of the outputs of the laser.

7.2.2 Mounting

The laser is mounted into a standard Vero moduel. The electrical terminals of the laser goes both to the front panel and to the rear connector of the Vero-frame. The connectors in the front is two D-sub9f. The pinout are according to the output of the laser controller and the temperature controller. A standard one-to-one cable can be used. The pin designations are

Laser pin	ITEM	Bias conn.	Temp conn.	Rear conn.
1	Temperature monitor	-	7	8a
2	Temperature monitor	-	8	8c
3	Laser DC bias (-)	1	-	-
4	Monitor(anode)	3	-	4a
5	Monitor(cathode)	4	-	4c
6	TEHP(+)	-	1,2	6a
7	TEHP(-)	-	3,4	6c
8	Gnd	9	-	10a/c
9	Gnd	9	-	10a/c
10	N.C.	-	-	10a/c
11	Laser ground	2	-	10a/c
12	Laser modulation(-)	-	-	-
13	Gnd	9	-	10a/c

(7.2)

The "Laser modulation(-)"- input is mounted at the front panel. The panel is shown in fig. 7.7.

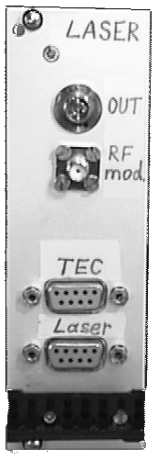

Figure 7.7: Frontpanel of Veroframe.

7.3 Temperature regulator and cryostat

The cryostat where the APD is sitting is equipped with an oven. The purpose of this is to adjust the temperature and raise it above the LN_2 boiling point.

Cryostat

The oven is a brass plate with ceramic isolated resistant wire. The fig.7.8 shows how the cryostat is made.

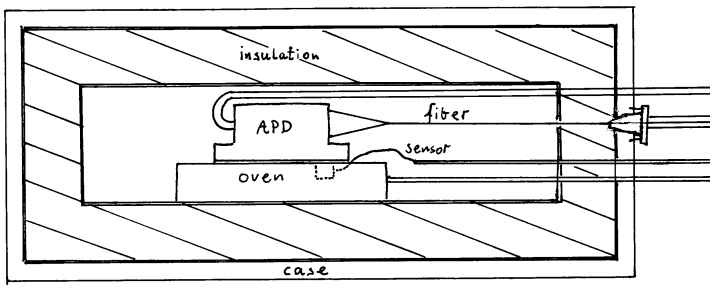

Figure 7.8: The cryostat, APD, sensor and oven.

The core of the cryostat is suspended by isolation material from its cold surroundings. Inside the core is the APD is mounted onto the oven and the sensor is sandwiched in between. The outer shell is an ordinary Eddystone box.

Temperature regulator system

A laser temperature regulator is connected to the sensor and the oven, and provides almost complete regulating system. Only an adaptor is needed. Fig.7.9 shown this

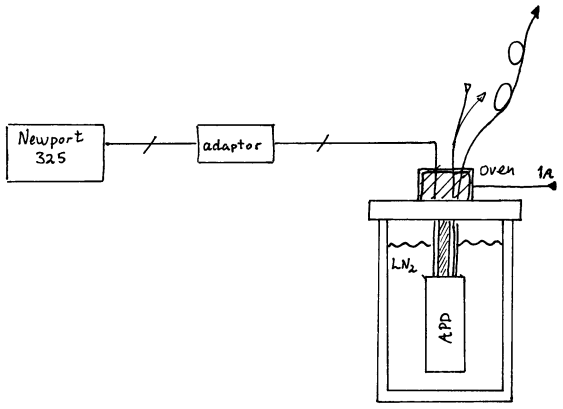

Figure 7.9: The cryostat is put into a bath of LN_2 in a big thermos container. The cryostat is made so that it is easy replaceable.

The top of the nitrogen container is also provided by an oven. This is top prevent icing if the wires and a current of 1A is run through this oven.

Adaptor

The laser temperature regulator, Newport 325, is supposed to regulate a Peltier element. This element is polarity sensitive and a current is always run through. The adaptor isolates the oven from positive current.

Without the presence of the adaptor the oven would be heating at all times. The temperature is set on the regulator as an ohmic value. By looking up in the table of appendix D the corresponding temperature can be looked up. Since the regulator only can heat the current will flow through the 5W resistor in the adaptor of wrong settings are made. An indicator LED will then glow. The connections are

Pin at reg.	Item	Pin at adaptor connector
1,2	Te+	1,2
3,4	Te-	4,5
7	Sensor+	3
8	Sensor-	center

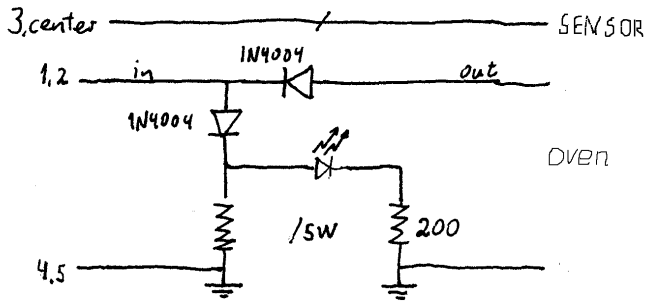

Figure 7.10: Adaptor circuitry with an indicator lampe for wrong settings.

Sensor

The sensor used is a platinum film PT1000 element. Any fabrication can be used as long it fits under the APD. This element is 2mm X 5mm.

7.4 Instruments

To conduct an identical experiment this information is included. The symbol -!- means that settings are changed during the experiment.

7.4.1 Connections

This diagram is also included here for reasons of convenience. Connections between the devices can be done by any 50Ω cable of about 1m of length. The lines marked with a T must be 9m.

7.4.2 Settings

HP54540A

Used to monitor the output of APD circuitry and to determine trigger level of the signal at the counter. The adjustments are user preferable, but this is approx. what they should be.

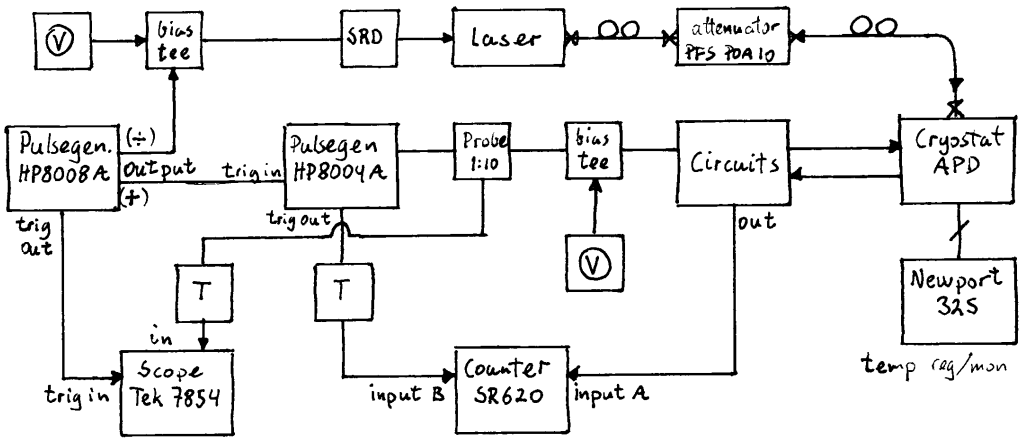

Figure 7.11: All the instruments connected for the experiment

Item	Setting	Units
V/div	100	mV
time/div	1	ns
trig	internal	

Tektronix 7458

Used as a monitor for the gate pulse and to characterize the laser pulse. A good, but tricky instrument. Some of the knobs and buttons are analog and don't show a reading at the display, and must be adjusted. There is only one input for signal and triggering at the 15GHz module.

Gate pulse monitor

Item	Setting	Units
V/div	100	mV
time/div	2	ns
trig	external	

Laser pulse characterization

Item	Setting	Units
V/div	10	mV
time/div	50	ps
trig	external	

Stanford Research SR620

The instrument was used both to count avalanches and make histograms. There is some outputs at the rear panel. A(ny) scope can monitor the histogram and the counting. A plotter can also be connected via the GPIB interface. Manual should be referred if doing experiments other that this.

Counting

Item	Setting	Units
Source	A	
Gate	1	s
Samlpe	10	
Input A	signal	trig:80mV

Histogram

Item	Setting	Units
Source	A	
Gate	+time	s
Samlpe	-!-(<5k)	
Input A	signal	trig: 80mV
Input B	trig	trig:200mV

HP8008A

The central unit for synchronization, frequency of system($f_{rep)}$ and pulse to SRD unit of laser.

Item	Setting	Units
Frequency	-!-	Hz
Trig	Internal	
Pulse width	2	ns
Pulse delay	5-20	ns
Output (-)	SRD-unit	amp: $\approx 3V$
Output (+)	trig HP8004	amp: $\approx 2V$
Trig out	Tek7458 trig	

Through a biasTee a bias is added to the pulses. The level of this is approx. 3.11V. The biasTee is sitting directly at the (-)connector of the pulse generator.

HP8004A

Provides the gate pulse to the APD.

Item	Setting	Units
Frequency	controlled by HP8008A	Hz
Trig	External	
Pulse width	4	ns
Pulse delay	1-10	ns
Output	APD circuitry	amp:-!-
Trig out	SR620 input B	

Through a biasTee a bias is added to the output pulses. The level of this is approx. 23-24 V. The biasTee is sitting directly at the connector of the pulse generator.

7.4.3 Identity

The instruments used are property of SINTEF and NTNU. They all have an unique inventory number that correspond to serial numbers of manufacturer. This is filed in the instrument archives.

Intrument	**Model**	**Inventory number**
Scope	HP 54540A	KA 5001
	Tektroniks 7458	KA 2027
Pulse generator	HP 8008A	JA 2024
	HP 8004A	AJ 2001
Counter	SR 620	AJ 3009
Temp.regulator	Newport 325	SE 3020
Laser driver	Light Inst. 502	FC 3105
Attenuator	PFS POA 10	
BiasTee	Picosecond Labs	2890 3/94
	Avtech AVX-T	1579
Multimeter	Keityly 174	GR 3049
Powersupply	GW GPS-3030	FC3121
	GW GPS-3030	FC3118

The rest of the instruments can be picked by chance.

Chapter 8

Experiment

8.1 Purpose of experiment

In the preliminary experiment the APD was tested for properties regarding dark current only. These properties were documented and related to the operational characteristics. Much of its behavior were understood. More interesting is it to look at the same measurements, only this time with photons present. By using statistics and the mathematical models from chap.5 the SPD properties can be evaluated.

8.2 Experimental setup

This experimental setup is made to measure the efficiency of the detector, dark counts and arrivals of avalanches. The gate pulse and the laser pulse is both synchronized so that they overlap. The HP8008A is the central unit, synchronizing the whole system. In addition to this it also makes the pulses to the laser in conjunction with the SRD unit. The other pulse generator, the HP8004A provides the gate pulses. The delay between the laser pulse and the gate is about 50ns. However, depending on which cables used this must be tuned. The tuning is done by using the delay functions at the generators. To obtain the correct delay the SR620 can be used to monitor the photo counts.

More about how the experiment is done, which settings that are used and other details are described in chap.7.

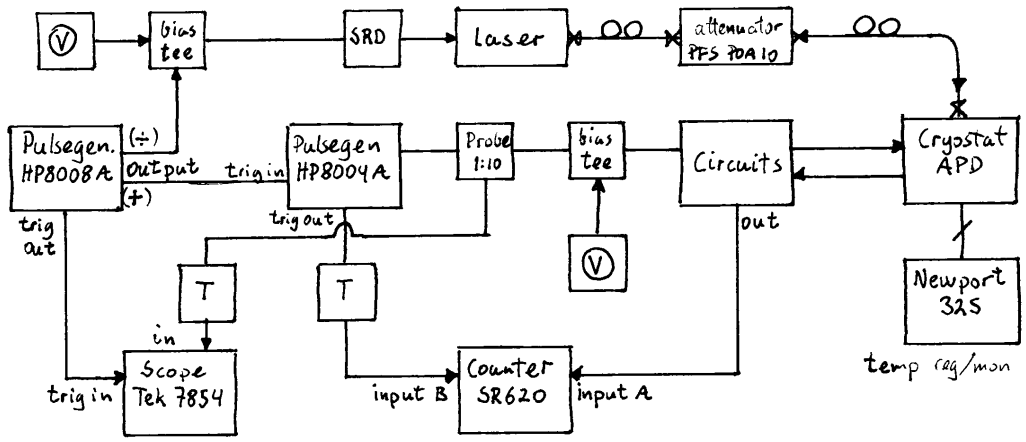

Figure 8.1: The experimental setup including both the APD and the laser.

8.3 Trials

Based on the preliminary measurements a set of measurements are decided. Due to low output amplitude of the gate pulse generator the variety of measurements are limited(new pulsegenerator is ordered).

8.3.1 Motivation

- The excess voltage should have two values to see how this affects detector efficiency and dark counts. The measurements should be made for a few values of the bias V_R to se how close it can be made V_B.
- The pulse efficiency of the laser should be made at two values to observe starting saturation and testing during the trial.
- These measurements should be made for different values of the rep.rate f_{rep}. To run the system at high f_{rep} is desirable
- To check if temperature has a beneficial effect there should be made a parallel series of measurements where the temperature is raised above the boiling point of LN_2.

8.3.2 Points

Two main trials are based on temperature, one for $-198°C$ and one for $-188°C$. The gate width is set to a fixed value of $4ns$. The measurements

made are best illustrated by the following tables.

Temp	Excess	B	i	a	s	V_R[V]:	
	volt.V_E[V]	23.6	23.8	24.0	24.2	24.4	24.6
$-198°C$	$V_E = 1$	1	2	3	-	-	-
	$V_E = 2$	4	5	6	-	-	-
$-188°C$	$V_E = 1$	-	-	-	7	8	9...
	$V_E = 2$	-	-	-	10	11	12

For all these points, except those marked (-), there were made the following measurements.

rep.rate[kHz]	darkcont	$\eta_{photon=}0.05$	$\eta_{photon} = 0.1$
50	a	g	m
100	b	h	n
200	c	i	o
300	d	j	p
500	e	k	q
800	f	l	r

In addition to this some histograms were made to show distribution of the photons. The filled in tables and histograms are included in the appendix.

8.4 Restrictions of the models

8.4.1 Problem

The models made in chap.5 are only valid when there is a linear dependence on the dark counts and the frequency. That is when trapping is not the major source to dark counts. If there is a significant contribution from trapping the detector efficiency can exceed 100%, which is indeed impossible. Some restrictions must therefore apply.

8.4.2 Plots

The dark counts are plotted versus the rep.rate. Since the QC system will operate at $\eta_{photon} = 0.1$ the corresponding dark count values are used in these plots. The plots are $V_E = 1$ in fig.8.2 and $V_E = 2$ in fig.8.3.

The plots for temp=$-188°C$ are very similar to fig.8.2 and fig.8.3. The linearity of the $V_E = 1$ curves decline at about $500kHz$ there the number of counts sharply rises. For the $V_E = 2$ the linearity is only valid up to about $200kHz$.

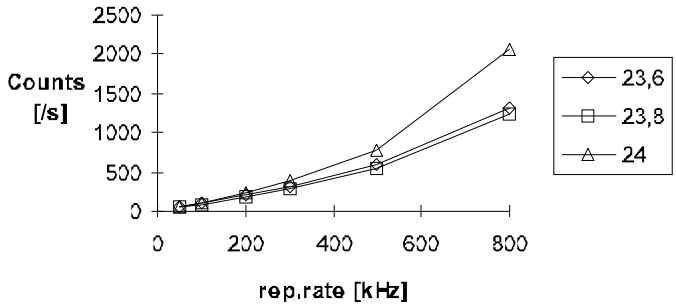

Figure 8.2: Dark count vs. rep.rate at V_E=1, temp=-198°C.

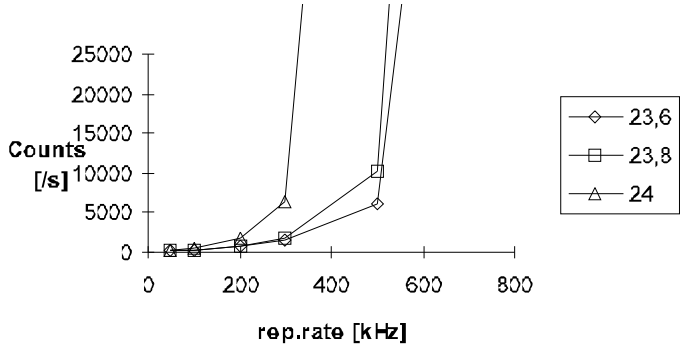

Figure 8.3: Dark count vs. rep.rate at V_E=2, temp=-198°C.

8.4.3 Discussion and conclusions

If thermally generated carriers are the major source to dark counts there should be a linear dependence on the dark count rate. When trapping in starting there are two components of the dark count rate. The dependence will therefore be a function of a higher order. This is explained in chap. 3 and observed in fig.8.2 and fig.8.3. Considering the linearity the models for $V_E = 1$ are good up to $500kHz$ and $V_E = 2$ up to $200kHz$. Since the number of counts sharply rises beyond the suggested limits the error rates will also increase correspondingly. The error rate will therefore be a good indicator to reveal any problem like this.

.

8.5 Analysis of the models

In this section it's decided what to do with the collected data. The models from chap.5 are discussed and analyzed. Three propertied will be investigated; temperature dependence, detector efficiency and detection efficiency. Included is also the error rate based on the dark counts. All models will be presented as diagrams.

8.5.1 Temperature

Temperature has several effects on the APD. However, the magnitude of the different effects are partly unknown. If the reachthrough voltage is larger than the breakdown voltage the APD will not achieve optimal operation. This can be changed by increasing the temperature, since the reachthrough voltage is not a function of temperature. Temperature also increases the rate of thermally generated carriers. If these effects are differently weighted we can expect different results. All dark count should be plotted in the same diagram.

8.5.2 Detector efficiency

Detector efficiency shows how good the detector is to detect single photons. This efficiency does only consider the properties of the detector.

$$\begin{aligned} \eta_{APD}(X, f_{rep}) &= \eta_{detected} \\ &= \left(\frac{\overline{n}_{detected} - \eta_{photon} \cdot \overline{n}_{dark}}{\eta_{photon} \cdot f_{rep}} \right) \end{aligned}$$

Loss in connectors and fiber is not included but the real value will then always be a little better than the one measured.

$$\begin{aligned} \eta_{detected} &= \eta_{QE} \cdot (connectors) \cdot (fiber) \\ &= \eta_{QE} \cdot d_{connector} \cdot d_{fiber} \end{aligned}$$

The error rate should also be included in the diagram. This will show the magnitude of the dark counts the of the specific operational parameters.

$$e(X, f_{rep}) = \left(\frac{\overline{n}_{dark}}{f_{rep}} \cdot 100\% \right)$$

8.5.3 Detection efficiency

From a system point of view it is interesting to talk about detection efficiency. Here, the utilization of time is also brought into consideration. The detector efficiency only investigates the isolated ability to detect single photons. The detection efficiency η_{SYSTEM} will tell how the system performs. The factor f_{max} is chosen to the highest value of f_{rep} and η_{SYSTEM} is therefore a relative expression.

$$\begin{aligned} \eta_{SYSTEM}(X, f_{rep}) &= \eta_{APD} \cdot \eta_{rep} \\ &= \left(\frac{\overline{n}_{detected} - \eta_{photon} \cdot \overline{n}_{dark}}{\eta_{photon} \cdot f_{rep}} \right) \cdot \left(\frac{f_{rep}}{f_{max}} \right) \end{aligned} \tag{8.1}$$

To make a complete analysis of the system the error rate should be included in the diagram at the secondary axis.

$$e(X, f_{rep}) = \left(\frac{\overline{n}_{dark}}{f_{rep}} \cdot 100\% \right)$$

8.6 Temperature

8.6.1 Plots

The diagram in fig.8.4 shows dark counts for all settings at $V_E = 1V$ of the operational characteristics. The breakdown voltage for temp$=-198°C$ is $24.1V$ while the one for temp$=-188°C$ is $24.7V$. Despite the $0.6V$ difference in V_B the bias voltages can be translated. In the legend of the diagram the corresponding bias voltages are: $23.6 \leftrightarrow 24.2$, $23.8 \leftrightarrow 24.4$ and $24.0 \leftrightarrow 24.6$.

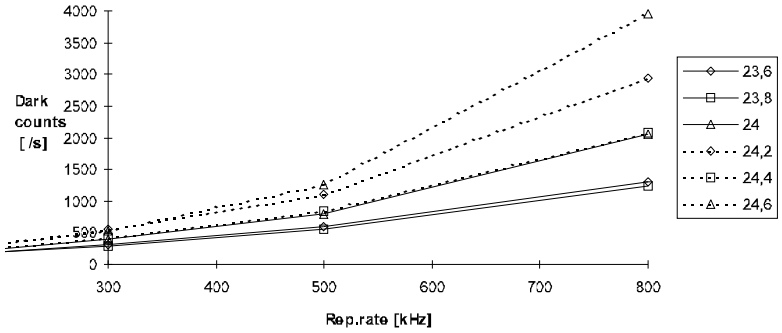

Figure 8.4: Dark current vs. rep.rate. The dotted curves are for temp$=-188°C$ and the solid are for temp$=-198°C$

8.6.2 Discussion and conclusion

If carefully studied, one can observe that the 24.0-curve are below the 24.2-curve. It should be located in between the 24.6 and the 24.2 curve. The most probable explanation is the broken detector. The curves for $V_E = 2V$ are very similar to fig.8.4 but saturation makes it hard to get any sense out of it.

No crossings of the curves in fig.8.4 can be observed. The crossings would have shown that the APD did not have optimal settings. The $-188°C$-curve would in the beginning be as measured here, but at some point cross the $-198°C$-curve. This could be explained that at higher temperatures there would be more thermally generated counts but the ability of reducing trapping was better.

This seems not to be the case and the elevation of temperature doesn't have any apparent effect on trapping. In general, raising of temperature increases the dark/trapping counts of this APD .

8.7 Detector efficiency

The detector efficiency are plotted based on the expression of $\eta_{APD}(X, f_{rep})$. In the same diagrams the error rate $e(X, f_{rep})$ is plotted in dotted curves. Since the models are limited by the rep.rate; $500kHz$ for $V_E = 1$ and $200kHz$ for $V_E = 2$ vertical marker are drawn in the diagrams. The values for temperature in the legends have the translation: $23.6 \leftrightarrow 24.2$, $23.8 \leftrightarrow 24.4$ and $24.0 \leftrightarrow 24.6$.

8.7.1 Plots

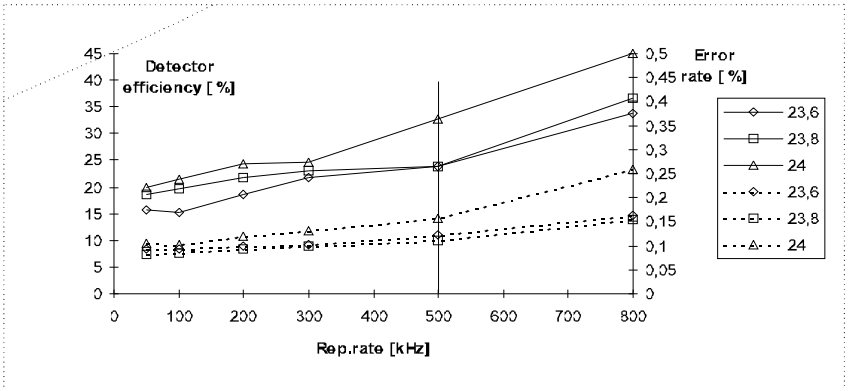

Figure 8.5: Detector efficiency and error rate for $V_E = 1$, temp$=-198°C$.

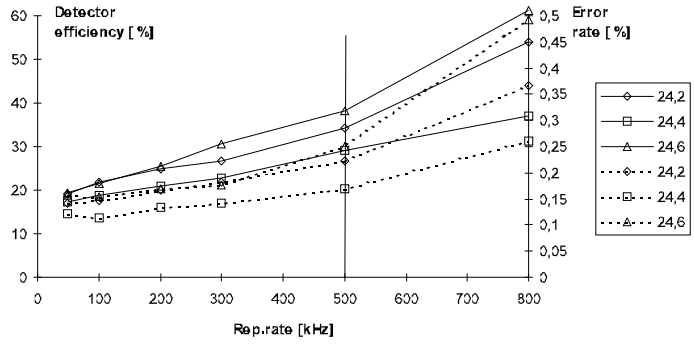

Figure 8.6: Detector efficiency and error rate for $V_E = 1$, temp$=-188°C$.

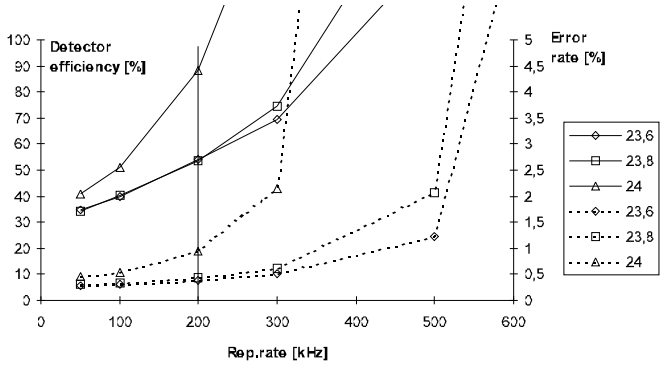

Figure 8.7: Detector efficiency and error rate for $V_E = 2$, temp$=-198°C$.

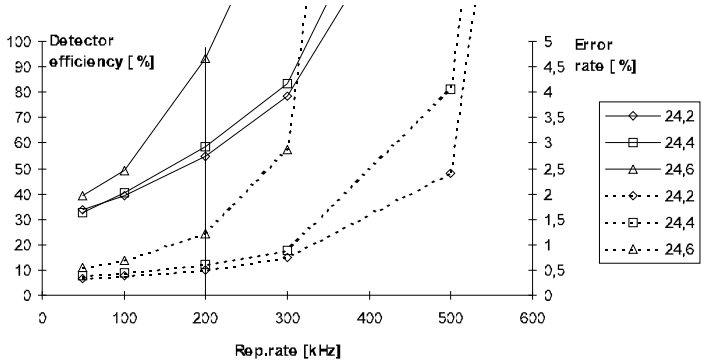

Figure 8.8: Detector efficiency and error rate for $V_E = 2$, temp$=-188°C$.

8.7.2 Discussion and conclusion

Error rate

The error rate for both $V_E = 1$-curves is almost constant up to a rep.rate of $500kHz$. The level of $-198°C$-curve is about 0.13%. The $-198°C$-curves has a small slope, starting at 0.15% and ending at 0.25%. This indicates that trapping is insignificant at low rep.rates and that the dark counts are due to thermally generated carriers. This also defines the lower boundary of time domain noise as dark counts can be considered as. Beyond $500kHz$ dark trapping starts to be significant, though for the $-198°C$-curves this doesn't seem so clear.

By increasing the excess voltage V_E, to $2V$ the quantum efficiency of the detector increases. So does the dark counts too. The error starts at an error rate a little less than 0.5%. Already at $200kHz$ the error rate starts rising to several percents. The result here doesn't differ from the ones in the preliminary results.

Detector efficiency

The detector efficiency for $V_E = 1$-curves follows the same course as the error rate. The levels are between $15\% - 20\%$ for the $V_E = 1$-curves. Beyond $500kHz$ the efficiencies increases due to trapping. It seems that the detector efficiency is a little better for the $-188°C$-curves, but this might be a result of more thermally generated carriers.

The $V_E = 2$-curves starts at $30\% - 40\%$ and quickly increases. The curves are similar for both temperatures. At the defined limit at $200kHz$ the detector efficiency is 90%. This might be a true result since the error rate of this point is about 1%, but starting trapping is also observed. Also, the V_R is very close to V_B.

The detection efficiency for lower values is 50% at $200kHz$ with a corresponding error rate of 0.5%. This is probably a more reliable magnitude of the efficiency since the error rate seems independent of the rep.rate which indicated that trapping is low or absent.

It also looks like the settings of V_R should not be closer that $0.2V$. The $V_R = 24.0$ curves show a significantly higher error rate that the one for lower values.

8.8 Detection efficiency

The detection efficiency are plotted based on the expression of $\eta_{SYSTEM}(X, f_{rep})$. In the same diagrams the error rate $e(X, f_{rep})$ is plotted. Since the models are limited by the rep.rate; $500kHz$ for $V_E = 1$ and $200kHz$ for $V_E = 2$ vertical marker are drawn in the diagrams. The values for bias in the legends have the same translation: $23.6 \leftrightarrow 24.2$, $23.8 \leftrightarrow 24.4$ and $24.0 \leftrightarrow 24.6$.

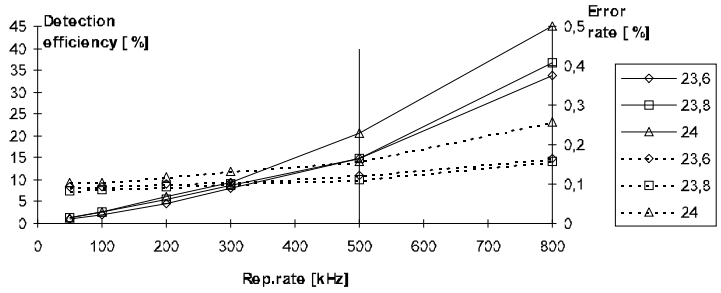

Figure 8.9: Detecion efficiency and error rate for $V_E = 1$, temp$=-198°C$.

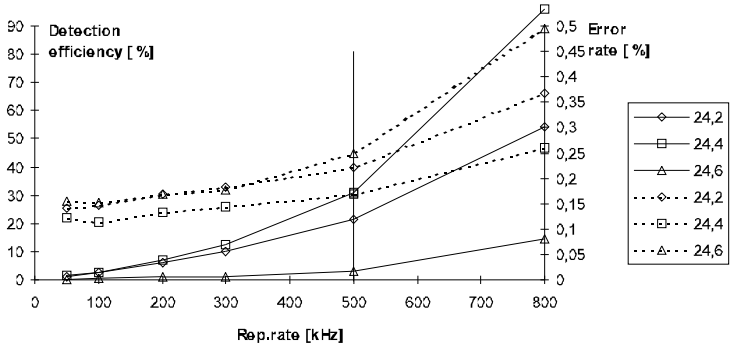

Figure 8.10: Detecion efficiency and error rate for $V_E = 1$, temp$=-188°C$.

8.8.1 Discussion and conclusion

Different detector efficiencies are demonstrated in the previous section. These efficiencies are obtained at various settings of the operational characteristics.

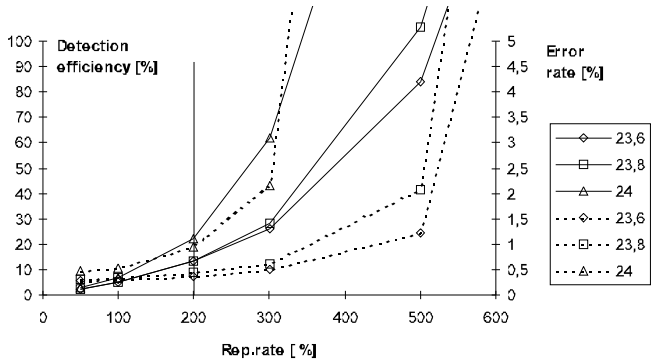

Figure 8.11: Detecion efficiency and error rate for $V_E = 2$, temp=$-198°C$.

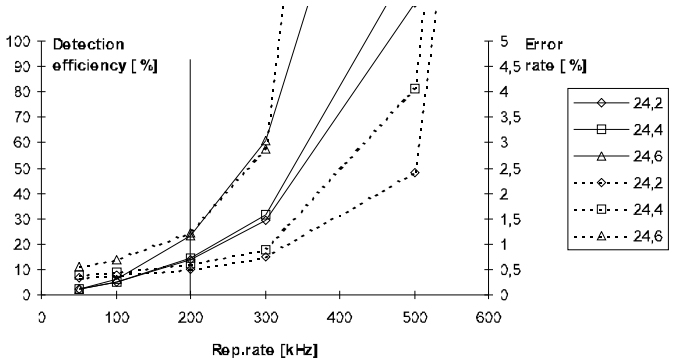

Figure 8.12: Detecion efficiency and error rate for $V_E = 2$, temp=$-188°C$.

Now the rep.rate is also brought into consideration. When trapping is low, that is at low rep.rates, the detection efficiencies are low for all plots. In absence of trapping the detection efficiency will increase with the rep.rate. This is clearly observed in fig.8.9. Here the error rate is constant up to $500kHz$(and even higher) while the efficiency is increasing. It it obvious what the settings should be. What is the point of a rep.rate when the error rate id the same at $50kHz$ and $500kHz$.

A detection efficiency of 35% is achieved at $500kHz$, while 50% at $200kHz$. From a detection efficiency point of view there is no difference of these two. Both achieve a detection efficiency of about 10%. That means that even they both transferee the same number of bits per. second. The 35%-settings gains at transmission speed while the 50%-settings gains at high detection rate. The loss is due to the opposite properties. To make a final decision where to put the settings the error rate must be considered. For the $V_E = 2$ settings the error rate is 0.5% while it is 0.25% for the $V_E = 1$ settings.

8.8.2 Histograms

Some histograms were made for selected settings of the operational parameters. They did not tell too much but was rather able to confirm some of the conclusions made. Due to the act of measurements the time scale is from right to lift.

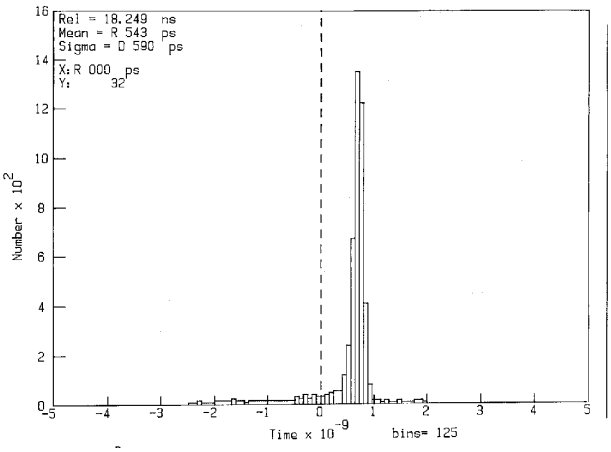

Figure 8.13: Most of the counts are photo generated

Most of the histograms were like this. When there was a low error rate and high detector efficiency the histograms looked the one in fig.8.13. This

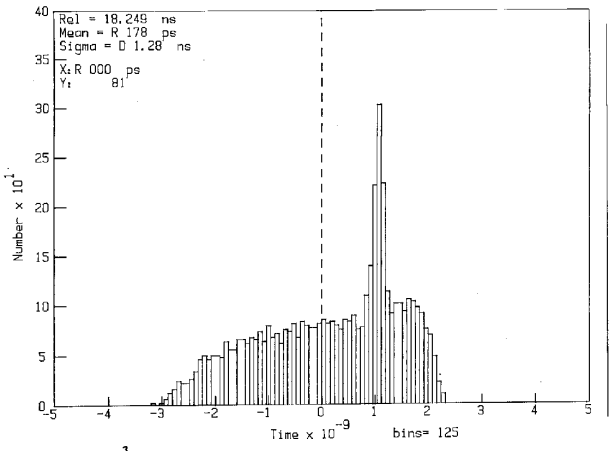

Figure 8.14: A mixure of dark counts and photo counts

histogram also shows the shape of the laser pulse. It's supposed to be 76ps FWHM. Here it is about 160ps. The reason for this is probably jitter in the system. Fig.8.13 shows when there is a large contribution of both photo counts and dark counts. Fig.8.15 shows the dark counts. The histogram also shows the shape of the gate pulse, at moderate number of dark counts. However, when trapping was significant this didn't show at the histograms. A exponential-like histogram had been expected.

8.9 The detector

The avalanche photodiode suddenly started to behave strange right before this trial. The dark counts and detector efficiency changed back and forth. This is probably because of thermal stress and optical misaligment was the most probable explanation. However, this did not explain the increased dark counts. Whitch conditions inside the APD that can cause this will only be speculations, impossible to confirm. The problem was solved by increasing the temperature some 10-20 degrees. Actually, an improvement could be monitored at the SR620 as the temerature went back to $-198°C$. This had to be done some times during the trials. Some figures might be incorreckt.

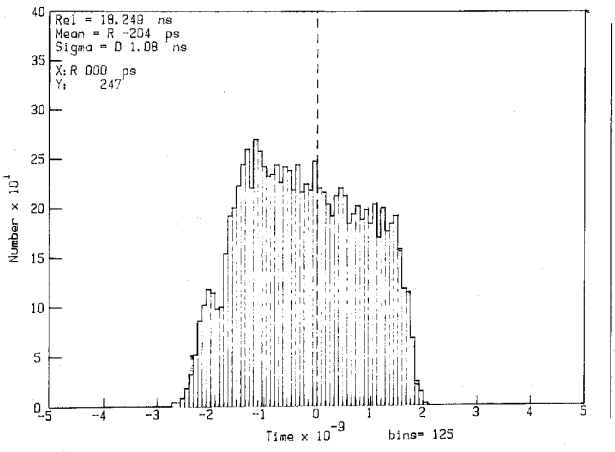

Figure 8.15: Dark current generated counts

Chapter 9

Conclusions

In this chapter the conclusions are rounded up and presented.

Two major sources of error were present. First, the detector behaved strangely. Probably it is about to be broken. The indication of this were that the dark counts and detector efficiencies at the same settings changed back and forth. By knocking at the cryostat and increasing the temperature the APD changed back to normal operation. When behaving strange the dark counts rose and the detection efficiency fell. There are for sure some points in the measurements that are measured under these conditions. However, it seems that most of the points are as expected.

The settings of the operational characteristics could influence the measurements. The rep.rate and the bias were under good control. The gate amplitude has a distorted shape and its width was a function of amplitude. This did not make it simple to get consistent measurements. The properties this would influence the most were the detection efficiency and the error rate(these properties are related). However, most of the measurements look reasonable, and this is probably not a source to any significant error, but rather a matter or precision of the numbers.

A incresement of the temperature was thought to have a beneficial effect on the APD. With this detector this did not seem to be the case. The dark counts increased and the detector efficiency was left almost unchanged. The little higher values measured can be caused by setting errors.

High detection efficiency were obtained. Figures as high as 50% were calculated and is considered to be correct. The error rate seemed independent on rep.rate. Also 90% efficiencies were obtained but there are reasons to doubt this result. It is measured beyond the point of starting trapping. Trapping caused a mathematical result of several hundred percent detector efficiency and some limitations were therefore applied.

It was first expected that a high excess voltage would be increase the

performance. The detection efficiency models revealed that this was not true. Actually, a lower excess voltage at low detection efficiency at high rep.rate can transferee as more bits at lover error rate that using settings with higher detection efficiencies.

However, this model does not give a obvious point of which settings to make. The user of the system must self determine which performance he/she wants. The models do give guidance where to put the settings.

Chapter 10

Appendix

Sett inn appendix fra WORD-dokument

Bibliography

[1] Paul Townsend Christophe Marand. Quantum key distribution over distances as long as 30 km. *Optics letters*, 20(16):1695–1697, 1995.

[2] Simon Phoenix Paul Townsend. Quantum cryptography: Secure communications using quantum cryptation. *British Telecommunications Engineering*, 16:207–213, 1997.

[3] Charles H. Bennett. Experimental quantum cryptography. *Journal of Cryptology*, 5:3–28, 1992.

[4] John M. Senior. *Optical Fiber Communications.* Prentice Hall International, 1992.

[5] B. Saleh/M. Teich. *Fundamentals of photonics.* Wiely Interscience, 1991.

[6] Ben G. Streetman. *Solid State Electronic Devics.* Prentice-Hall International, 4 edition, 1995.

[7] Technical Staff of CSELT. *Fiber Optic Communications Handbook.* TAB Professional and Reference Books, 1990.

[8] S.Cova A. Lacaita, F. Zappa and P.Lovati. Single-photon detection beyond 1um: persormance of commercially available ingaas/inp detectors. *Applied Optics*, 35(16):2986–2996, 1996.